Daniel Tianhou Zhang

The First Steps Towards a Perturbation Theory for Small Systems

June 2020

Master's thesis

Master's thesis

2020

Daniel Tianhou Zhang

NTNU
Norwegian University of
Science and Technology

NTNU
Norwegian University of
Science and Technology

NTNU
Norwegian University of
Science and Technology

The First Steps Towards a Perturbation Theory for Small Systems

Daniel Tianhou Zhang

Norwegian University of Science and Technology
Department of Chemistry

Acknowledgements

Abstract

Equation of State (EOS) developed from perturbation theory are well known in the literature and can be a very useful tool for modelling fluid behaviour. While popular perturbation theories of i.e. Barker-Henderson (BH) prove to be accurate for macroscopic pure-component fluids at high temperatures, there currently exist a lack of successful methods to obtain accurate EOS for fluids in small confinements. This thesis therefore investigates the applicability of BH perturbation theory (BHPT) for fluids confined to small systems, and extends the BHPT of the first order to the specific case of the Lennard-Jones/spline (LJ/s) fluid confined to small spherical geometries with hard walls. The investigation demonstrates two major findings, 1) a difference between small and bulk hard-sphere (HS) pressure and radial distribution function $g(r)$ (RDF) and 2) particles are depleted from the inner-core (IC) of the spherical confined HS fluid, which is adsorbed on the confinement wall. For the HS RDF $g(r)$, instead of tending towards $g(r) \to 1$ when the pair-distance $r \to \infty$, the small HS RDF reduces to zero when r equals the sphere confinement diameter. For the adsorption, the depletion causes a reduction in the IC density of the small system fluid, causing the fluid to exert properties more similar to bulk fluids with lower fluid densities. By taking these observations into account, a "small" first-order BHPT framework is developed and is observed to accurately predict the simulated first-order perturbation term a_1 and the simulated small HS and LJ/s pressures. By only requiring the bulk HS RDF, the adsorption per surface area Γ as a function of fluid density and the spherical ideal gas RDF, the small BHPT can predict small LJ/s properties under spherical confinement of any "relatively large" radius size R. "Relatively large" in the context of small systems means spherical confinement geometries that are large enough to give the confined fluid distinctive IC and outer-core (OC) structural regions, as the current small BHPT will break down when the regions cannot be told apart. While this thesis has investigated the LJ/s fluid, the small BHPT should be applicable for a variety of pair potentials, in addition to being able to be extended to other types of confinement geometries.

Sammendrag

Tilstandsligninger (EOS) utviklet gjennom perturbasjonsteori er kjent i litteraturen og kan være et nyttig verktøy for å modellere væskeoppførsel. Selv om populære perturbasjonsteorier av f.eks. Barker-Henderson (BH) fungerer nøyaktig for makroskopiske ren-komponentvæsker ved høye temperaturer, er det for øyeblikket en mangel av slike metoder for å oppnå nøyaktig EOS for væsker i små systemer. Oppgaven til denne masteroppgaven handler derfor om å undersøke i hvilken grad man kan bruke generell BH perturbasjonsteori (BHPT) til å utvikle EOS for fluider i små systemer, i tillegg til å utvide førsteordens BHPT til det spesifikke eksempelet av Lennard-Jones/spline (LJ/s) væsken begrenset inne i små sfæriske geometrier med harde vegger. Oppgaven viser to hovedfunn, 1) det finnes en forskjell mellom små og stor (bulk) hardkule (HS) trykk og radiell distribusjonsfunksjon $g(r)$ (RDF) og 2) den indre delen (IC) av den sfæriske geometrien mister partikler, der partiklene blir adsorbert på geometriveggen. For HS RDF $g(r)$, i stedet for å tendere mot $g(r) \rightarrow 1$ når paravstanden $r \rightarrow \infty$, så reduserer den små HS RDF til null når r tilsvarer sfære-geometri diameteren. Adsorpsjonen fører til en reduksjon av IC tettheten, noe som får væsken til å utøve egenskaper mer lik bulk væsker med lavere væsketetthet. Ved å ta hensyn til disse variablene, kan et "små" førsteordens BHPT-rammeverk utvikles, som viser seg å være nøyaktig til å prediktere første-ordens leddet a1, i tillegg til små HS og LJ/s trykk. Ved å bare kreve bulk HS RDF, adsorpsjon per overflate areal som funksjon av væsketetthet og den sfæriske ideell gass RDF, kan den små BHPT predikere små LJ/s væskeegenskaper i små systemer av sfæriske geometri av hvilken som helst "relativt stor" radius. "Relativt stor" i dette tilfellet betyr sfæriske geometrier som er stort nokk til å gi fluidene separate IC og ytre kjerne (OC) strukturelle geometrier, siden det nåværende rammeverket vil bryte sammen når man ikke kan skille regionene sammen. Selv om denne masteroppgaven har undersøkt LJ/s væsken, vil denne teorien være aktuell for en rekke parpotensialer, i tillegg til å kunne bli utvidet til andre systemgeometrier.

Contents

List of Figures

Nomenclature

Abbreviations

EOS   Equation of State

VDW   Van der Waals

HS   Hard Sphere

LJ   Lennard-Jones

LJ/s   Lennard-Jones/spline

MD   Molecular Dynamics

BH   Barker-Henderson

BHPT   BH Perturbation Theory

RDF   Radial Distribution Function

CS   Carnahan Starling

PHS   Pseudo Hard Sphere

PY   Percus-Yevick

BT   Bulk Transformation

IC   Inner-Core

OC   Outer-Core

ID   Ideal Gas

RES   Residual

AVG   Average

Symbols

N, n_{mol} Number of particles

$P, P^* = P\sigma^3/\epsilon$ Pressure

V Volume

T, T^* Temperature

$\mathcal{H}$ Hamiltonian

K_N Kinetic energy

U_N, W_N Potential energy

Q_N Partition function

Z_N Configuration integral

A, a Helmholtz energy

Λ de Broglie thermal wavelength

h Planck's constant

k_B Boltzmann's constant

m Mass

t Time

$\mathbf{r^N}, \mathbf{r_i}$ Cartesian coordinates

$\mathbf{p^N}, \mathbf{p_i}$ Momentum vector

$\mathbf{v}$ Velocity vector

B_n Virial coefficients

η Packing fraction

$\rho, \rho^* = \rho\sigma^3$ Number density

r Pair-distance

$u(r), w(r)$ Pair Potential

$g(r)$ Radial distribution function

$b_{\text{VDW},1}, b_{\text{VDW},2}$ VDW EOS parameters

σ, ε LJ parameters

$p_i, r_c, r_s, r_c, b_{\text{LJ/s},1}, b_{\text{LJ/s},2}, x_{\text{LJ/s}}$ LJ/s parameters

d HS diameter

Z_{CS} CS compressibility factor

R Spherical confinement radius

x, y, z Cartesian coordinates

g_0 Analytical spherical RDF

$h(k), n(k), n_k, n_c, k$ RDF variables

Γ Particle adsorption per surface area

D, h_c derivation variables

S_R, S_r, S_D Spheres R, r, D

A_R, A_r, A_D Surface area for S_R, S_r, S_D

x_0 Bulk transformation parameter

α, γ, λ Perturbation variables

F Force

$\rho_N^{(n)}$ Equilibrium n-particle density

1 Introduction

Many fields require in-depth understanding of fluid behaviour for a large spectrum of pressure and temperature values. At the same time, obtaining data from experiments can be difficult due to high costs and demanding experimental conditions. A theoretical alternative is to develop analytical expressions that can predict the behaviour of fluids with a certain degree of accuracy. These expressions are called Equation of States (EOS) and are defined as equations that relates pressure P with volume V and temperature T of homogeneous systems at thermodynamic equilibrium [3]. Methods to obtain EOS are currently well established for pure fluids that can be characterized by classical thermodynamics, i.e. bulk fluids with a volume V and particle number N large enough to cause variables variables such as V and N to be extensive. One example of such an expression is the Van der Waals (VDW) EOS that relates thermodynamic state variables in the following way

$$\left(P + b_{\mathrm{WDV,1}} \frac{n_{\mathrm{mol}}^2}{V^2} \right) (V - n_{\mathrm{mol}} b_{\mathrm{WDV,2}}) = n_{\mathrm{mol}} RT \tag{1.1}$$

where n_{mol} is the number of particles in moles and R is the gas constant. In comparison to the ideal gas law EOS that models fictive, volumeless particles without particle-particle interactions, the VDW EOS introduces two additional variables $b_{\mathrm{VDW,1}}$ and $b_{\mathrm{VDW,2}}$ that characterize attractive intermolecular interactions and particle volume. To derive the EOS, VDW treated intermolecular interactions as mathematical pair potentials with attractive and repulsive regions that gives particles volume and particle-particle attraction [4]. Examples of pair potentials include the comprehensively studied hard-sphere (HS) and Lennard Jones (LJ) pair potentials, where HS purely exerts short-range hard repulsion representing particle volume, while LJ additionally exerts long-range weak attraction representing particle-particle attraction. To finally obtain Equation 1.1, VDW recognized that fluid structure is primarily determined by the particle volume, and therefore simple fluids with molecular interactions can be accurately approximated to purely have HS fluid structure with an additional uniform "background" attraction governing particle movement. More accurate methods to obtain EOS have been developed since then based on the same idea. Examples include the cubic Redlich-Kwong [5] and Peng–Robinson [6] EOS, and also the more sophisticated Barker Henderson perturbation theory (BHPT) EOS [7].

While these methods have been proven to be very useful in the many areas that require accurate data for fluids of bulk size, the predictability of macroscopic EOS can possibly decease for fluids of nanoscale, as finite-size effects become prominent with decreasing fluid volume [8]. Examples of finite-size fluid-systems include confined fluids in random porous media [9] and nano-encapsulated phase-changing materials [10], where fluid properties can be additionally dependent on the factors such as confinement geometry and surface tension. In addition to the recent interest in nanotechnology development, a key area of interest is therefore to investigate how well macroscopic EOS can predict nanofluid properties and to possibly establish EOS that can accurately model nanoscale fluids. Examples of ongoing EOS developments within the topic include modelling fluids in random porous media using scaled particle theory [11] [12] and extending the VDW EOS to pure fluids in confined cylinders [13]. A topic that have not been researched in depth however, is how well BHPT can be applied and extended to isolated nanofluids in confinement.

The purpose of this master thesis is therefore to investigate the topic of EOS that can describe the behaviour of confined nanofluids, where the specific research objective is to investigate and extend the general first-order BHPT to the simple case of the Lennard-Jones/spline (LJ/s) fluid confined to small, spherical confinement geometries with hard walls. Completing this objective will provide the first steps towards accurate EOS representations for confined nanofluids using BHPT. The objective will primarily be accomplished through theoretical developments and molecular dynamics (MD) simulations in LAMMPS [14] for LJ/s particles in spherical small-systems without periodic boundary conditions. Non-periodicity in this thesis means that no particles exist outside the spherical confinement. The first objective is to obtain simulated properties of the LJ/s fluid in spherical confinement, followed by applying and extending BHPT to such systems. The thesis body will consist of theory, thermodynamic methods, results and discussion followed by a few concluding remarks and a few future work suggestions.

Since this thesis will investigate theoretical fluids confined to small systems in LJ units of σ and ϵ, the terms "small", "smallness" and "finite-size" would better describe the investigated systems in comparison to less arbitrary terms such as "nano" or "nanoscale". On the other hand, "bulk" will therefore denote macroscopic and large systems at the thermodynamic limit. A more in-depth discussion on the definition of "small" and "bulk" is explained in Section 2.47.

2 Theoretical Background

This chapter will present the necessary background theory to investigate and obtain a method to determine EOS that can describe the behaviour of confined fluids in small spherical geometries based on the general BHPT. The chapter begins by introducing classical fluids in terms of excess Helmholtz energy, pair potentials, fluid structure and molecular dynamics, followed by a an overview of the general Barker-Henderson perturbation theory. Then an overview of the definition on small systems will be presented. Lastly, a spherical ideal gas RDF that was developed under the thesis investigation is presented, as the spherical ideal gas RDF proved to be an essential factor to obtain small EOS.

2.1 Excess Helmholtz Energy

Consider a one-component system characterized by N spherical particles with a diameter d and mass m interacting together at a temperature T inside a volume V. At a time t, the system will be completely specified by $3N$ coordinates $\mathbf{r}^N \equiv \mathbf{r}_1, ..., \mathbf{r}_N$ and $3N$ momentum vectors $\mathbf{p}^N \equiv \mathbf{p}_1, ..., \mathbf{p}_N$ of the particles. The total energy of the system can be described by the hamiltonian $\mathcal{H}$, which is expressed as the sum of the kinetic energy of all N particles $K_N\left(\mathbf{p}^N\right)$ and the potential energy that arises from intermolecular particle interactions $U_N\left(\mathbf{r}^N\right)$

$$\mathcal{H}\left(\mathbf{r}^N, \mathbf{p}^N\right) = K_N\left(\mathbf{p}^N\right) + U_N\left(\mathbf{r}^N\right) \tag{2.1}$$

where

$$K_N = \sum_{i=1}^{N} \frac{|\mathbf{p}_i|^2}{2m} \tag{2.2}$$

and

$$U_N\left(\mathbf{r}^N\right) = \sum_i^N u_e\left(\mathbf{r}_i\right) + \sum_i^N \sum_{j>i}^N u\left(\mathbf{r}_i, \mathbf{r}_j\right) + \sum_i^N \sum_{j>i}^N \sum_{k>j}^N u_t\left(\mathbf{r}_i, \mathbf{r}_j, \mathbf{r}_k\right) + \ldots \tag{2.3}$$

The term $u_e\left(\mathbf{r}_i\right)$ represents the interaction that occurs when the system of particles are exposed to an external field, while the terms $u\left(\mathbf{r}_i, \mathbf{r}_k\right)$, $u_t\left(\mathbf{r}_i, \mathbf{r}_j, \mathbf{r}_k\right)$ and so on represents the particle interactions. Under conditions when the external field potential equals zero and when the triplet $u_t\left(\mathbf{r}_i, \mathbf{r}_j, \mathbf{r}_k\right)$ and higher order particle interactions are neglected, the

potential energy reduces to a functional of the pair potential function $u\left(\mathbf{r}_i, \mathbf{r}_k\right)$

$$U_N\left(\mathbf{r}^N\right) \approx \sum_i^N \sum_{j>i}^N u\left(\mathbf{r}_i, \mathbf{r}_j\right) \tag{2.4}$$

The partition function Q_N for the NVT ensemble can be expressed as

$$Q_N = \frac{1}{h^{3N} N!} \iint \exp(-\beta\mathcal{H})\mathrm{d}\mathbf{r}^N \mathrm{d}\mathbf{p}^N \tag{2.5}$$

where h is Plank's constant, k_B is Boltzmann's constant and $\beta = 1/(k_B T)$. The momentum integral of the partition function can be solved exactly

$$Q_N = \frac{1}{h^{3N} N!} \int \exp\left(-\beta U_N\right)\mathbf{r}^N \int_{-\infty}^{\infty} \exp(-\beta \sum_{i=1}^N \frac{|\mathbf{p}_i|^2}{2m})\mathbf{p}^N = \frac{1}{N!} \frac{Z_N}{\Lambda^{3N}} \tag{2.6}$$

where Λ is de Broglie thermal wavelength and Z_N is the configurational integral

$$\Lambda = \left(\frac{2\pi\beta\hbar^2}{m}\right)^{1/2} \tag{2.7}$$

$$Z_N = \int \exp\left(-\beta U_N\right)\mathrm{d}\mathbf{r}^N \tag{2.8}$$

When the intermolecular potential is zero, $u\left(\mathbf{r}_i, \mathbf{r}_j\right) = 0$, the system reduces to ideal gas conditions such that the ideal gas configuration integral becomes

$$Z_N^{\mathrm{id}} = \int \cdots \int \mathrm{d}\mathbf{r}_1 \cdots \mathbf{r}_N = V^N \tag{2.9}$$

$$Q_N^{\mathrm{id}} = \frac{1}{N!} \frac{V^N}{\Lambda^{3N}} \tag{2.10}$$

The partition function can as a result be expressed as

$$Q_N = Q_N^{\mathrm{id}} \frac{Z_N}{V^N} = Q_N^{\mathrm{id}} Q_N^{\mathrm{res}} \tag{2.11}$$

The partition functions connects statistical mechanics to thermodynamics. The Helmholtz free energy can therefore be expressed as a function of the ideal and residual NVT partition functions

$$A(N, V, T) = -k_B T \ln Q_N = -k_B T \ln Q_N^{\mathrm{id}} - k_B T \ln Q_N^{\mathrm{res}} \tag{2.12}$$

The primary goal of these derivations is to prove that the total Helmholtz free energy can be separated into a sum of the more known "ideal" part and an "residual" part by equivalently stating

$$a = \frac{A}{Nk_BT} = \frac{1}{Nk_BT}\left(A_{\text{id}} + A_{\text{res}}\right) = a_{\text{id}} + a_{\text{res}} \tag{2.13}$$

An expression for the complete Helmholtz free energy a corresponds to an EOS that completely describes the fluid characterized by the pair potential $u\left(\mathbf{r}_i, \mathbf{r}_j\right)$. By using Stirling's factorial approximation $\ln N! \approx N \ln N - N$, the ideal Helmholtz free energy part can be expressed as

$$a_{\text{id}} = \frac{A_{\text{id}}}{Nk_BT} = \ln \Lambda^3 \rho - 1 \tag{2.14}$$

The ideal term is readily evaluated while the residual term is not. A topic of interest is therefore to develop methods that can obtain accurate expressions for a_{res}, a term that arises from the consideration of intermolecular interactions defined by the pair potential $u\left(\mathbf{r}_i, \mathbf{r}_j\right)$. One of the methods to obtain a_{res} is through BHPT, where the residual Helmholtz energy is approximated into a reference hard repulsion part and a series of perturbations. Before explaining BHPT in Section 2.4, the fluid structure and the pair potentials $u\left(\mathbf{r}_i, \mathbf{r}_j\right)$ relevant to this thesis will be introduced first.

2.2 Fluid Structure & Radial Distribution Function

It can be shown that the equilibrium n-particle density $\rho_N^{(n)}$ is defined as Equation 2.15 for canonical systems [15]

$$\rho_N^{(n)} = \frac{N!}{(N-n)!}\frac{1}{Z_N}\int \exp\left(-\beta U_N\right) \mathrm{d}\mathbf{r}^{(N-n)} \tag{2.15}$$

where the product of the single-particle density $\rho_N^{(1)}(\mathbf{r})$ and a volume element $\mathrm{d}\mathbf{r}$ determines the average number of particles in that volume element. The total number of particles in the system can be obtained by integrating over all space

$$\int \rho_N^{(1)}(\mathbf{r})\mathrm{d}\mathbf{r} = N \tag{2.16}$$

The single-particle density of a uniform fluid is therefore equal to the overall number density

$$\rho_N^{(1)}(\mathbf{r}) = N/V = \rho \tag{2.17}$$

For the case of $n = 2$, the product $\rho_N^{(2)}(\mathbf{r}_1, \mathbf{r}_2)\, \mathrm{d}\mathbf{r}_1 \mathrm{d}\mathbf{r}_2$ can be interpreted as the average number of particle-pairs occupying the volume elements $\mathrm{d}\mathbf{r}_1 \mathrm{d}\mathbf{r}_2$. For the special case of a uniform, ideal gas, the pair density $\rho_N^{(2)}$ becomes

$$\rho_N^{(2)} = N(N-1)\frac{1}{V^N}V^{N-2} = \frac{1}{\rho^2}\left(1 - \frac{1}{N}\right) \tag{2.18}$$

For homogeneous systems, the the pair-particle distribution function $g_N^{(2)}(\mathbf{r_1}, \mathbf{r_2})$ can be defined as

$$g_N^{(2)}(\mathbf{r_1}, \mathbf{r_2}) = \frac{\rho^{(2)}(\mathbf{r}_1, \mathbf{r}_2)}{\rho^{(1)}(\mathbf{r}_1)\,\rho^{(1)}(\mathbf{r}_2)} \tag{2.19}$$

If the system is also isotropic, then the pair distribution function $g_N^{(2)}(\mathrm{d}\mathbf{r_1}\mathrm{d}\mathbf{r_2})$ becomes a function of only the pair-distance separation $r_{1,2} = \|\mathbf{r_1} - \mathbf{r_2}\|$, and is usually called the radial distribution function $g(r)$ (RDF). When r is much larger than the range of the pair potential, the radial distribution function approaches the ideal gas limit (Equation 2.18), such that $g(r) \to 1$ when $r \to \infty$ and N is a large number. The radial distribution function $g(r)$ provides a fundamental method to describe local fluid structure by describing the probability of finding a particle at a distance r from any arbitrary reference particle in the system relative to the ideal gas distribution. Since the ideal gas is structureless, the ideal gas RDF always equals 1. Figure 2.1a displays the particle distribution for an ideal gas and Figure 2.1b displays the particle distribution for a very structured fluid (2D).

(a)   (b)
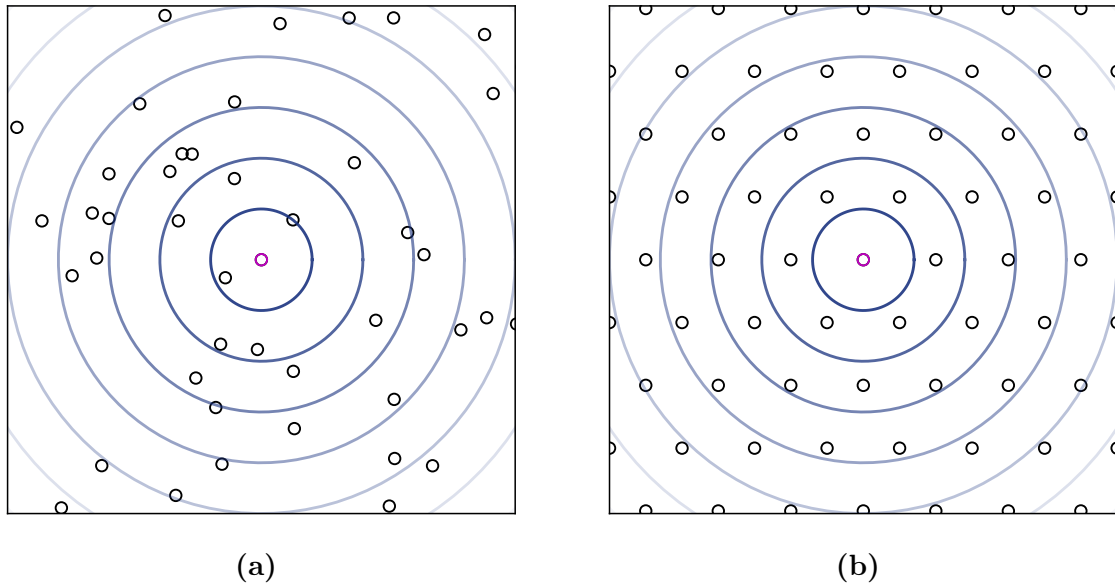
Figure 2.1: Illustrations of (a) an ideal gas configuration and (b) a very structured fluid. The concentric circles represent different values of the pair-distance r, where the pair-distance between the magenta and black particles can (a) have any value on average for the ideal gas case and (b) can have distinct values due to particle volume and structure. The figures are strictly illustrative, and were made in Python.

Compared to an ideal gas RDF, the RDF of real fluids will exhibit more oscillatory behaviour with successive maxima and minima due to particle volume and packing effects. This can be seen from Figure 2.1b, where oscillatory behaviour can be represented by the concentric circles and empty space around any reference particle, which is a consequence of strongly repulsive forces at short distances. Figure 2.2 displays the radial distribution function for the HS fluid as a function of the pair-distance r [1].
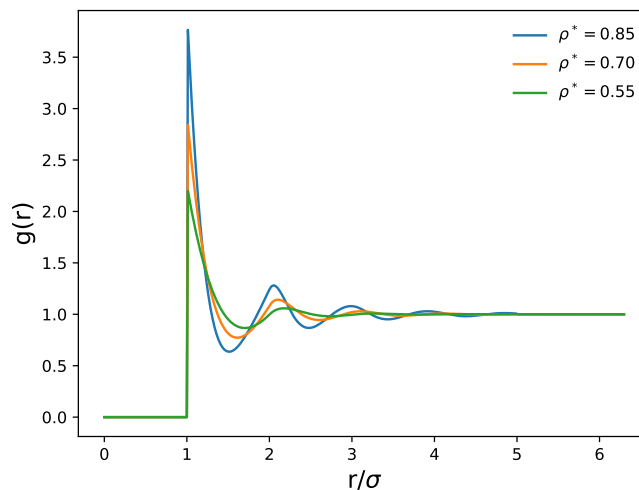
Figure 2.2: The analytical bulk Percus-Yevick HS RDF [1] at three densities with HS diameter $d_{\mathrm{HS}} = 1\sigma$.

The RDF equals zero from 0 to σ for $d_{\mathrm{HS}} = 1\sigma$ as the probability of finding a particle within the radius of a HS particle equals zero. The successive peaks represents the probability of finding a particle at a distance of the concentric circles of neighbor particles, i.e. $g(r) = 3$ represents the probability of finding 3 particles at the distance r. The pair distribution is very useful for obtaining thermodynamic properties for fluids with packing and structure effects.

2.3 Pair Potentials

Pair potentials are mathematical functions that describe the potential energy between two particles given their relative pair-distance in space $r = \|\mathbf{r_1} - \mathbf{r_2}\|$, such that $u(\mathbf{r_1}, \mathbf{r_2}) = u(r)$. As a consequence, pair potentials can describe pair-potential fluids, where the particle behaviour are governed by the potential. In terms of fluid perturbation theory, the main principle is to approximate a complicated pair potential fluid into a simpler, solvable reference fluid, such that a series of perturbations make up the difference between the two fluids. For this thesis, the reference fluid is governed by the HS pair potential while the

investigated fluid is governed by the LJ/s pair potential. The following sub-sub-sections will therefore present the relevant pair potentials for the HS and LJ/s fluids and their bulk EOS, in addition to the wall potential used for spherical confinement.

2.3.1   Reference Pair Potentials

One of the more simpler pair potential fluids is the hard-sphere fluid, which can be described as three-dimensional spherical particles with a certain diameter d that cannot overlap in space. The behaviour can be mathematically stated by the hard-sphere intermolecular pair potential $u_{HS}(r)$

$$u_{HS}(r) = \begin{cases} \infty & \text{for } r < d \\ 0 & \text{for } r \geq d \end{cases} \tag{2.20}$$

where the sole interaction between the hard-sphere particles is that they become impenetrable at $r = d_{\text{HS}}$, the HS diameter. A method to obtain the HS EOS is by determining all the virial coefficients B_n in the infinite virial series expansions of the compressibility factor Z, defined as

$$Z = \frac{PV}{Nk_BT} = 1 + \sum_{n=2}^{\infty} B_n \rho^{n-1} = 1 + B_2\rho + B_3\rho^2 + \dots \tag{2.21}$$

Unfortunately, only the first number of virial coefficients can be determined analytically. A consequence is therefore that an exact solution for the hard-sphere equation of state does not currently exist. The fact that the EOS for essentially an ideal gas fluid with volume has to be approximated, illustrates the difficulty in modelling fluid behaviour. A popular and accurate hard-sphere equation of state used in this thesis is called the Carnahan-Starling (CS) EOS [16]. The EOS can be obtained by approximating the virial coefficients as a simple algebraic expression, such that

$$B_n \approx \left(n^2 + n - 2\right) = 4, 10, 18, \dots \quad n \geq 2 \tag{2.22}$$

where B_n is the nth hard-sphere virial coefficient and $n \geq 2$. For illustration, the 2nd to 4th exact hard sphere virial coefficients are 4, 10 and 18.3647684 respectively [17]. By summing to an infinite order, the following hard-sphere equation of state is obtained in terms of the HS compressibility factor Z_{CS}

$$Z_{CS} = \frac{1 + \eta + \eta^2 - \eta^3}{(1 - \eta)^3} \tag{2.23}$$

where $\eta = \pi\sigma^3\rho/6$ is the packing fraction. The resulting equation is found to predict pressures that are virtually indistinguishable from computer simulation pressures obtained over the entire fluid range [16]. The residual hard-sphere contribution to the Helmholtz energy can be obtained by using the following expression [18]

$$
\begin{aligned}
A_{HS} = A - A_{\mathrm{id}} &= \int_\infty^V (P - \frac{Nk_BT}{V})\mathrm{d}V \\
&= -Nk_BT \int_0^\eta \frac{1}{\eta}\left(Z_{CS} - 1\right)\mathrm{d}\eta = Nk_BT\frac{4\eta - 3\eta^2}{(1-\eta)^2}
\end{aligned}
\tag{2.24}
$$

in reduced form

$$
a_{HS} = \frac{A_{HS}}{Nk_BT} = \frac{4\eta - 3\eta^2}{(1-\eta)^2}
\tag{2.25}
$$

One of the more efficient methods to simulate HS in MD is to use the discontinuous MD framework [19], a framework that "off-the-shelf" MD codes such as LAMMPS do not currently have. As a consequence, obtaining simulated HS properties can be difficult when only LAMMPS is accessible. A work-around is to use an empirical Mie pair potential, also called the Pseudo HS pair potential (PHS) to approximate HS fluid behaviour, which is documented to accurately reproduce HS properties at $T^* = 1.5$ [19]

$$
u_{PHS}(r) =
\begin{cases}
50\left(\frac{50}{49}\right)^{49}\epsilon\left[\left(\frac{\sigma}{r}\right)^{50} - \left(\frac{\sigma}{r}\right)^{49}\right] + \epsilon & r < \left(\frac{50}{49}\right)\sigma \\
0 & r \geq \left(\frac{50}{49}\right)\sigma
\end{cases}
\tag{2.26}
$$

This pair potential will be used to reproduce HS properties from LAMMPS simulation in this thesis. Both the HS and PHS potentials are plotted together in Figure 2.3
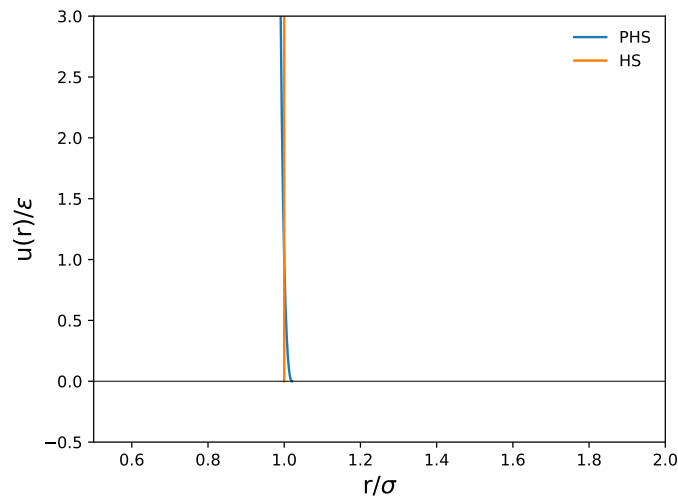
Figure 2.3: The HS and PHS pair potentials as a function of pair-distance, as seen in Equations 2.20 and 2.26. Both potentials represent the HS particles with $d_{\mathrm{HS}} = 1\sigma$.

2.3.2   LJ and LJ/s Pair Potentials

In comparison to the discontinuous HS pair potential, a more realistic pair potential
can be constructed to imitate neutral, real atoms by expressing the short-range Pauli
repulsion as r^{-12} and long range van der Waals attraction as r^{-6} [15]. By combining
the two contributions in the following way, the Lennard-Jones pair potential $u_{LJ}(r)$ is
obtained

$$u_{LJ}(r) = 4\varepsilon\left[\left(\frac{\sigma}{r}\right)^{12} - \left(\frac{\sigma}{r}\right)^{6}\right] \tag{2.27}$$

where ϵ is the depth of the attractive potential well and σ is the distance at which the
pair potential reduces to zero. A difficulty with such a pair potential is the intrinsic
large computational power required to simulate the virtually zero forces that arise for all
particles when r tends to infinity. In other words, every Lennard-Jones particle is always
affected by the other N-1 particles independent of the distance. An alternative method to
avoid such an issue is to truncate the Lennard-Jones pair potential with a spline, a cubic
polynomial that reduces to zero at a more reasonable distance. The Lennard-Jones/spline
pair potential $u_{LJ/s}(r)$ can be expressed as

$$u_{LJ/s}(r) = \begin{cases} 4\varepsilon\left[\left(\frac{\sigma}{r}\right)^{12} - \left(\frac{\sigma}{r}\right)^{6}\right] & \text{for } r < r_s \\ b_{\text{LJ/s},1}\left(r - r_c\right)^2 + b_{\text{LJ/s},2}\left(r - r_c\right)^3 & \text{for } r_s < r < r_c \\ 0 & \text{for } r > r_c \end{cases} \tag{2.28}$$

where $r_s = \left(\frac{26}{7}\right)^{1/6}\sigma$, $r_c = \frac{67}{48}r_s$, $b_{\text{LJ/s},1} = -\frac{24192}{3211}(\epsilon/r_s^2)$ and $b_{\text{LJ/s},2} = -\frac{387072}{61009}(\epsilon/r_s^3)$. The
distance r_c gives the Lennard-Jones inflection point and the parameters a, b and r_c are
determined such that the potential and the derivative are continues at r_s and r_c. As
a result of this truncation, the Lennard-Jones/spline pair potential becomes zero at r_c
instead of tending to zero as r tends to infinity. Compared to hard-spheres, obtaining an
accurate EOS for LJ or LJ/s fluids can be considerably more difficult due to the more
complex pair potential. As mentioned previously, thermodynamic perturbation theories
such as the BHPT have been developed to produce EOS for pair potentials like LJ and
LJ/s, and will be presented in later sections. Here the first order perturbation term for a
bulk LJ/s EOS is presented, which is obtained from the general BHPT

$$\begin{aligned} A_1/N = a_1 = 2\pi\epsilon k_B T\rho^*\Big[&p_1(\rho^*)^4 + p_2(\rho^*)^3 + p_3(\rho^*)^2 + p_4(\rho^*) + p_5 + (\rho^*)(p_6(\rho^*)^2 \\ &+ p_7(\rho^*) + p_8)(x_{\text{LJ/s}} - 1) + (\rho^*)(p_9(\rho^*)^2 + p_{10}(\rho^*) + p_{11})(x_{\text{LJ/s}} - 1)^2\Big] \end{aligned} \tag{2.29}$$

i	p_i	i	p_i	i	p_i	i	p_i
1	0.04605	4	-0.3464	7	9.4890	10	-45.88
2	20.4554	5	-0.5351	8	0.5337	11	4.6270
3	-0.3328	6	-7.529	9	30.73		

Table 2.1: Parameters for Equation (2.29)

where $\rho^* = N\sigma^3/V$ is the reduced density, p_i are parameter values listed in Table 2.1 and $x_{\mathrm{LJ/s}} = \sigma/d$. The expression is obtained by correlating the two-dimensional polynomial $a_1/(2\pi\epsilon k_B T \rho^*)$ against 5 isotherms $T^* \in \{0.4, 0.7, 0.85, 1.0, 2.0\}$ and $0 < \rho^* < 0.9$ [20].

In terms of simulating fluids in a confined geometry in LAMMPS, a wall-potential can be defined to keep particles from escaping the geometry confinement. A hard wall is desired in this thesis. Constrained to LAMMPS' WALL/REGION command however, completely hard walls cannot be exerted to the spherical confinement system. Instead the following cut and shifted LJ pair potential is used as a "pseudo-hard" confinement wall potential, which can also be called as the WCA pair potential

$$u_{WCA}(r) = \begin{cases} 3 \times 4\varepsilon \left(\left(\frac{0.01\sigma}{r}\right)^{12} - \left(\frac{0.01\sigma}{r}\right)^6 \right) + 3\varepsilon & \text{for } r < 0.01 \times 2^{1/6}\sigma \\ 0 & \text{for } r \geq 0.01 \times 2^{1/6}\sigma \end{cases} \quad (2.30)$$

The comparison between the LJ and LJ/s pair potential is shown in Figure 2.4a, and the wall-potential is shown in Figure 2.4b

(a)

(b)
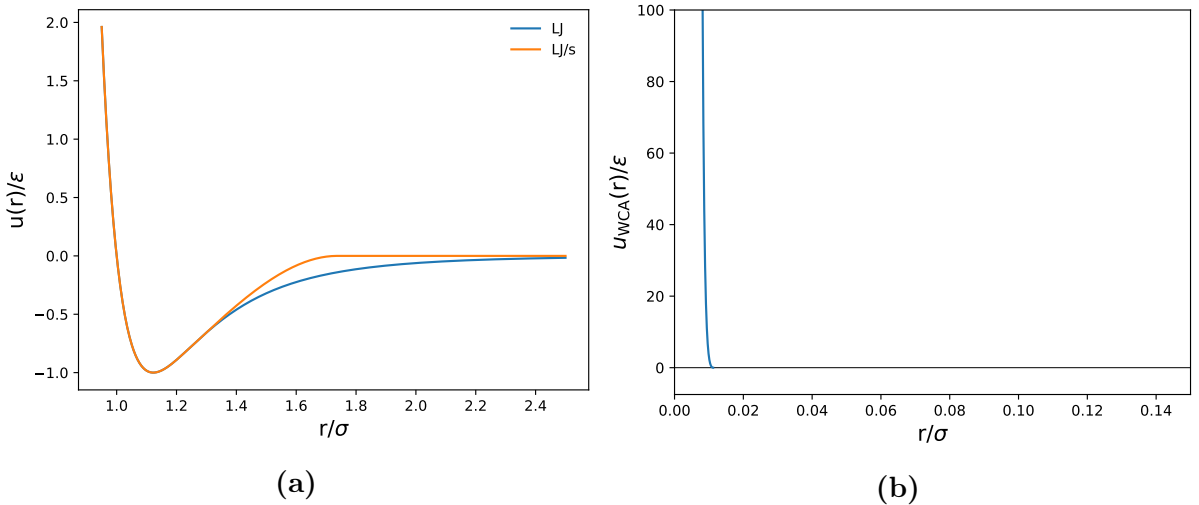
Figure 2.4: (a) The LJ and LJ/s pair potentials from Equations 2.27 and 2.28, (b) the WCA wall-potential as a function of pair-distance r from Equation 2.30.

2.4   Thermodynamic Perturbation Theory

The essence of perturbation theory is to approximate the solution of a difficult problem as the solution of a related, simpler problem plus additional small "perturbation" terms that characterize the difference between the two problems. In practice, the difficult problem of obtaining a LJ/s EOS can be solved by obtaining the EOS for a solvable reference system plus a number of pertubative terms. The perturbation theory used in this thesis is the BHPT, which assigns HS fluids as the reference system. The theory starts by defining a modified pair potential $u_{BH}(d, \sigma, \alpha, \gamma\, r)$ expressed through the target pair potential $u(r)$ as

$$u_{BH}(d, \sigma, \alpha, \gamma; r) = \begin{cases} u[d + (r - d)/\alpha] & \text{for } d + (r - d)/\alpha < \sigma \\ 0 & \text{for } \sigma < d + (r - d)/\alpha < d + (\sigma - d)/\alpha \\ \gamma u(r) & \text{for } \sigma < r \end{cases}$$

(2.31)

where α varies the steepness of the modified potential in the repulsive region and γ varies the depth of the potential well in the attractive region. The modified potential reduces to the HS potential $u_{HS}(r)$ with diameter d when $\alpha = \gamma = 0$ while original potential $u(r)$ is recovered when $\alpha = \gamma = 1$. By expanding the Helmholtz energy for the modified potential $u_{BH}(r)$ in a double Taylor series in α and γ around the point $\alpha = \gamma = 0$, the following expression is obtained from Equation 2.12

$$\beta A_{\text{res}} = -\ln Q_N^{\text{res}}\big|_{\alpha=\gamma=0} - \alpha \left.\frac{\partial \ln Q_N^{\text{res}}}{\partial \alpha}\right|_{\alpha=\gamma=0} - \gamma \left.\frac{\partial \ln Q_N^{\text{res}}}{\partial \gamma}\right|_{\alpha=\gamma=0} + \dots$$

(2.32)

The first term in the Taylor series equals the HS Helmholtz energy A_{HS}. By evaluating Equation (2.32) at $\alpha = \gamma = 1$, the complete residual Helmholtz energy for $u(r)$ can be recovered as a sum of the HS Helmholtz energy A_{HS} and an infinite series of perturbations A_1, A_2 and so on. The final result from the double Taylor expansion can be expressed as

$$\begin{aligned} \frac{A_{\text{res}}}{NkT} = {}& \frac{A_{HS}}{NkT} - 2\pi\rho d^2 g_0(d) \left(d - \int_0^\sigma \{1 - \exp[-\beta u(z)]\} dz \right) \\ & + 2\pi\rho\beta \int_\sigma^\infty g_0(r) u(r) r^2 \mathrm{d}r + \text{ higher-order terms} \end{aligned}$$

(2.33)

where ρ is the number density. As can be seen, the HS diameter d influences both the hard-sphere particle-size and the overall perturbative Helmholtz energy. By defining the

HS diameter d_{HS} in Equation 2.34

$$d_{BH}(T) = \int_0^\sigma \{1 - \exp\left(-\frac{u(z)}{k_B T}\right)\}\mathrm{d}z \tag{2.34}$$

then the first of the two first-order perturbation terms in Equation 2.33 will reduce to zero, causing the HS diameter d_{HS} to become temperature dependent according to BHPT. The final expression for $A_{\mathrm{res}}/(Nk_B T)$ will therefore equal

$$\frac{A_{\mathrm{res}}}{Nk_B T} = \frac{A_{HS}}{Nk_B T} + 2\pi\rho\beta \int_\sigma^\infty g_0(r)u(r)r^2\mathrm{d}r + \text{ higher-order terms} \tag{2.35}$$

where the first perturbation term a_1 is

$$a_{1,\mathrm{RDF}} = 2\pi\rho \int_\sigma^\infty g_0(r)u(r)r^2\mathrm{d}r \tag{2.36}$$

The subscript RDF in $a_{1,\mathrm{RDF}}$ denotes that a_1 is obtained by integrating the RDF using Equation 2.36. The complete set of perturbations can be expressed as an expansion over $\beta = (k_B T)^{-1}$ [2] such that the reduced residual Helmholtz energy a_{res} can be expressed as

$$a_{\mathrm{res}} = a_{HS} + \beta a_1 + \ldots\ldots = \sum_{n=0}^\infty (\beta)^n a_n \tag{2.37}$$

where

$$a_{\mathrm{res}} = \frac{A_{\mathrm{res}}}{Nk_B T} \qquad\qquad a_{HS} = \frac{A_{HS}}{Nk_B T} \tag{2.38}$$

Increasing the temperature would therefore decrease the magnitude of higher order perturbation terms, making the first order BHPT EOS to be more accurate. This form of residual Helmholtz energy expansion has been derived previously in 1954 by Zwanzig [21], which takes basis in splitting the target potential $u(r)$ into a reference system pair potential $u_0(r)$ plus a perturbation potential $w(r_{ij}; \lambda)$ governed by a coupling parameter λ that has a value between 0 and 1. The simplest case occurs when

$$u_\lambda(r_{ij}) = u_0(r_{ij}) + \lambda w(r_{ij}) \tag{2.39}$$

where

$$u_0(r) = \begin{cases} u(r) & r \le \sigma \\ 0 & r > \sigma \end{cases} \qquad\qquad w(r) = \begin{cases} 0 & r \le \sigma \\ u(r) & r > \sigma \end{cases} \tag{2.40}$$

The total perturbation energy from the pair potential $w(r)$ can be expressed as

$$W_N(\mathbf{r}^N) = \sum_{i=1}^{N} \sum_{j>1}^{N} w(r_{i,j}) \tag{2.41}$$

By performing a λ-expansion using Equation 2.12, Equation 2.37 can be obtained. Another result from the λ-expansion is that the first-order perturbation term a_1 can also be expressed as a statistical average of the attractive contribution of the target potential [22]

$$a_{1,\mathrm{AVG}} = \frac{\langle W_N \rangle}{N} \tag{2.42}$$

Equation 2.42 provides an important alternative method to obtain the first order perturbation term a_1, as statistical averages can be obtained directly from molecular simulation methods.

2.5   Molecular Dynamics

A short introduction to computational molecular dynamics will be presented in this section. Classical molecular dynamics is a computational method to simulate particle dynamics by solving Newton's equations of motion for N interacting particles

$$m_i \frac{\partial^2 \boldsymbol{r}_i}{\partial t^2} = \boldsymbol{F}_i, i = 1 \ldots N \tag{2.43}$$

where m_i, $\mathbf{r}_i$ and $\mathbf{F}_i$ are particle i's mass, position and force. The forces $\boldsymbol{F}_i$ are the negative derivatives of the particles' potential function $U_N(\mathbf{r}^N)$. The particles' positions and velocities can be obtained as a function of time by numerically solving Newton's equations of motion for a small time step Δt. An accurate and stable method to integrate Equation 2.43 is by using the velocity Verlet integrator, which expresses particles' time-dependent positions and velocities as

$$\begin{aligned}
\boldsymbol{v}\left(t + \frac{1}{2}\Delta t\right) &= \boldsymbol{v}(t) + \frac{\Delta t}{2m}\boldsymbol{F}(t) \\
\boldsymbol{r}(t + \Delta t) &= \boldsymbol{r}(t) + \Delta t \boldsymbol{v}\left(t + \frac{1}{2}\Delta t\right) \\
\boldsymbol{v}(t + \Delta t) &= \boldsymbol{v}\left(t + \frac{1}{2}\Delta t\right) + \frac{\Delta t}{2m}\boldsymbol{F}(t + \Delta t)
\end{aligned} \tag{2.44}$$

By initializing the particles with initial coordinates and velocities, the system will usually reach an equilibrium state after a certain number of time steps. When considering MD simulations in the NVT ensemble, the number of particles N, the volume of the system V and the temperature T remains constant while energy can be exchanged with the environment. Keeping the system at a constant temperature is a non-trivial task however, as the system temperature is directly related to the kinetic energy of the particles. A frequently used algorithm to control the temperature is called the Nosé-Hoover thermostat, which introduces a friction factor that slows down or accelerates particles until the temperature is equal to the desired value. After an "initialization" run to equilibrate the system, a "production" run can be performed to obtain macroscopic properties by averaging equilibrium configurations of the system. An alternative to simulating a large number of particles is to implement periodic boundary conditions to mimic macroscopic fluid behaviour. More specifically, periodic boundary conditions convert the simulation system into an "unit cell" with an "infinite" number of unit cell neighbors, such that when a particle passes through one side of the unit cell, it will re-appear on the opposite side with the same velocity. Periodic boundary conditions are desired when the objective is to simulate bulk fluids. This is visually explained in Figure 2.5
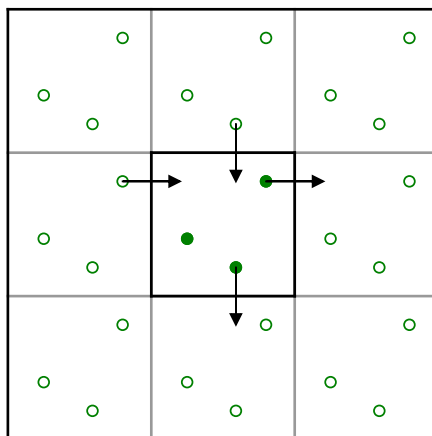
Figure 2.5: A two-dimensional snapshot of periodic simulation cells. Molecules that "leave" the center cell in one direction, will return to the same cell in the other direction.

A complication with periodic boundary conditions occurs when simulating particles with long-range pair-potentials, as the long-range interactions will cause disarray for the particle dynamics between unit cells.

2.6   Thermodynamics of Small Systems

In thermodynamics, the main difference between fluids confined to "small" and "bulk" sized volume confinements are their surface area to volume ratio. For fluid volumes with radius R, the ratio becomes

$$\text{ratio} = \frac{4\pi R^2}{(4/3)\pi R^3} = 3/R \tag{2.45}$$

Bulk fluids with N and V values of large size will minimize the ratio value ($R \to \infty$), causing any surface effects exerted to the fluid to be negligible in comparison to the effects exerted by the fluid body. That way, the Helmholtz energy of the bulk fluid system can be seen to be extensive in terms of variables such as N and V, where increasing N and V by a factor of i.e. 2 can be seen as doubling the system's total Helmholtz energy in the NVT ensemble

$$A\left(2N, 2V, T\right) = 2A\left(N, V, T\right) \tag{2.46}$$

On the other hand, the surface area to volume ratio becomes much larger for small systems ($R << \infty$), causing surface effects to play a significant role to the fluid behaviour in small systems. That way, doubling N and V cannot be seen as doubling the total Helmholtz energy. Because macroscopic bulk systems does not consider smallness effects, bulk thermodynamic properties cannot be directly comparable to properties of small systems [23]. Therefore, fluids confined to small systems can be defined as systems that experience finite-size effects, in addition to having variables such as N and V to no longer be extensive.

Since the first order bulk LJ/s BHPT EOS is readily obtainable, the task in this thesis is to investigate how surface effects alter the BHPT terms a_{HS} and a_1 in Equation 2.47 when LJ/s fluids are confined to small spherical systems with hard walls. The ideal gas EOS a_{ID} is independent of the volume size, as ideal gas particles have no finite-size effects in the first place. A difference between the small and bulk terms should be observed since the bulk LJ/s EOS does not consider finite-size effects.

$$a_{\text{LJ/s}} \approx a_{\text{ID}} + a_{\text{HS}} + \beta a_1 \tag{2.47}$$

2.7 Analytical Circle Equation

One of the more interesting results obtained from simulations on fluids confined to small spherical geometries, is the specific shape of the RDF. Instead of tending towards $g(r) \to 1$ when $r \to \infty$, the small RDF reduces to zero when r equals the sphere confinement diameter, as seen in Figure 2.6
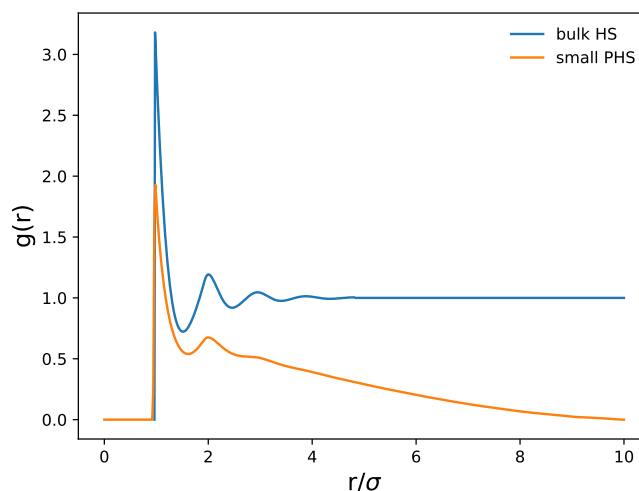
Figure 2.6: The bulk HS and small PHS RDFs at $\rho^* = 0.85$ and $d_{\mathrm{HS}} = 0.96424\sigma$ as a function of pair-distance r. The Bulk HS RDF is obtained from the analytical Percus-Yevick expression [1] while the small PHS RDF is obtained from LAMMPS simulation. The small system has a spherical radius of $R = 5\sigma$.

One of the main causes for such a reduction is that no particle pairs can have a separation higher than the confinement diameter for non-periodic conditions. Other causes for the reduction can be due to an altered fluid packing effect caused by the confined walls. However, given that the non-periodicity factor is the only contributor to the small RDF behaviour, then an interesting expression to obtain is an analytical equation that purely describes the non-periodicity effect. In other words, what kind of behaviour would the non-periodic RDF for a fluid confined to a spherical geometry exhibit if the fluid structure is unaffected by confinement geometry? Such an analytical equation can be derived for the ideal gas, as ideal gas have no volume or intermolecular interactions contribution to fluid structure. At the same time, the pure "non-periodic" effect can still be observed due to the fact that no ideal gas particles exist outside the confinement for small systems. This section will therefore provide a full derivation for the spherically confined ideal gas RDF, $g_0(r)$. To the best of our knowledge, this is the first time $g_0(r)$ have been derived in the open literature. The derivation of $g_0(r)$ has therefore been a part of the thesis work.

First, the term "non-periodic" in relation to RDFs can be explained. Non-periodicity is a MD term that simply means that the simulated unit-cell of particles will not be replicated an infinite number of times to mimic the behaviour of bulk fluids, as explained in Section 2.5 and Figure 2.5. In a more general sense, non-periodicity means that no particles will exist outside the confinement geometry. This will be the thesis definition of "non-periodic". Systems with periodicity will therefore mean bulk fluids. The comparison between a periodic and non-periodic fluid is illustrated in Figure 2.7a, where no particles can exist in the grey area for non-periodic spherical systems. The effect that non-periodicity has on the RDF calculation can be explained through an example: Given an arbitrary (black) particle inside a spherical confinement, the number of neighbor particles that the black particle can have at a pair-distance r (the distance between the black and colored circle), will be reduced from all the particles that lie on the colored sphere, to the sum of particles inside the non-shaded area. Increasing the pair-distance r will decrease the number of possible neighbor particles that can be sampled. Therefore, given any particle within the fluid, $g_0(r)$ will give a probability lower than the equivalent bulk RDF, in addition to giving zero probability of finding a neighbor particle at a pair-distance of the confinement diameter or higher. The confinement sphere in the this thesis and the following derivation is defined as a sphere S_R with a radius R.

The key step in this derivation is to define a sphere S_r with the pair-distance value r as its radius, such that the reduction in the number of available pair-distances / neighbor particles at the pair-distance value r for an arbitrary particle, becomes proportional with the reduction in the available surface area of sphere S_r, A_r, inside the the confinement. This can be seen in the perimeter reduction in the 2D case in Figure 2.7a, where the magenta part of the sphere S_r surface area represents the possible sampled number of pair-distances for a non-periodic system. Therefore, for that black particle, instead of having to count the number of particles that fall into a volume shell of $r \pm \delta r$, only its reduced surface area of sphere S_r has to be calculated instead. The system variables are illustrated in Figure 2.7b, where x_i, D and h_c will be defined later.

In terms of the RDF calculation, calculating the reduced surface area for sphere S_r for an arbitrary particle within the confinement will depend on two factors, a) how close the particle is to the confinement wall and b) the pair-distance magnitude r as illustrated in Figures 2.8a and 2.8b
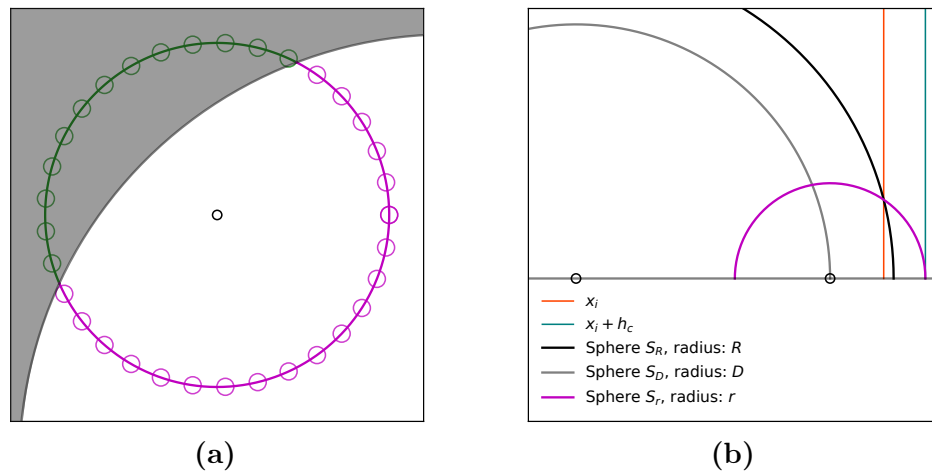
Figure 2.7: (a) A snapshot of a possible particle distribution around an arbitrary (black) particle at a certain pair-distance. When the fluid is confined to a spherical geometry, the particles in the grey area become separated from the particles inside the confinement, and will not be counted towards the RDF calculation. (b) Illustration of a spherical confinement system S_R with radius R. The centers of the variable spheres S_D and S_r are a distance D apart. The pair-distance r dictates the intersection point x_i and the spherical cap height h between spheres S_R and S_r.
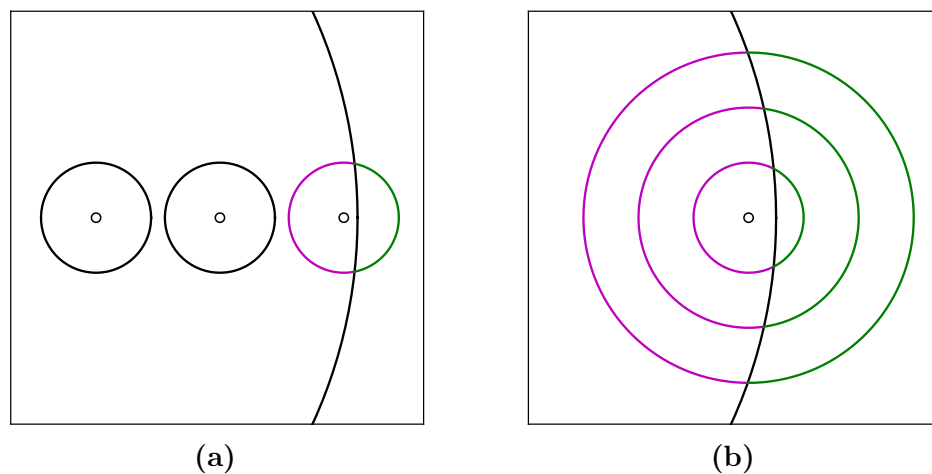
Figure 2.8: (a) Three particles inside a spherical confinement. Given the same pair-distance r, only the the particle closest to the wall will experience a reduction in the possible number of pair-distances that can be sampled. (b) Given a particle close to the confinement wall, the number of the possible sampled pair-distances will reduce with higher pair-distance magnitude r.

Next, the relevant values for the pair-distance r will be between $r \in 0 \leq r \leq 2R$, and the possible position values that a particle can have from sphere S_R's center is defined as D with a value between $D \in 0 \leq D \leq R$. The variable D will then define an additional sphere S_D with radius D that shares the the same center as sphere S_R. As mentioned previously, the sphere S_r surface reduction is directly related to its D magnitude. A specific property for spherical confinement is that all particles that lie on sphere S_D's surface, will experience the same reduction in surface area, as seen in Figure 2.9a.

Then, a function that describes the position of ideal gas particles inside the confinement is required. Given a pair-distance r, the reduction in S_r's surface area is only dependent on how far away particles are from the sphere S_R center. Since ideal gas particles will be evenly distributed throughout the whole confinement sphere, the number of particles that are a distance D away from the confinement sphere S_R center, will be assumed to be directly proportional to the surface area of sphere S_D, $A_D = 4\pi D^2$. For example, a higher number of ideal gas particles will lie on a larger A_D than a smaller A_D. A normalized comparison between the the surface area of sphere S_D and the experimental number of particles as a function of D is plotted in Figure 2.9b. The consequence of this function is that the number of particles at a certain distance D away from the sphere S_R center can be obtained, where all the particles has the same reduction in surface area S_r.
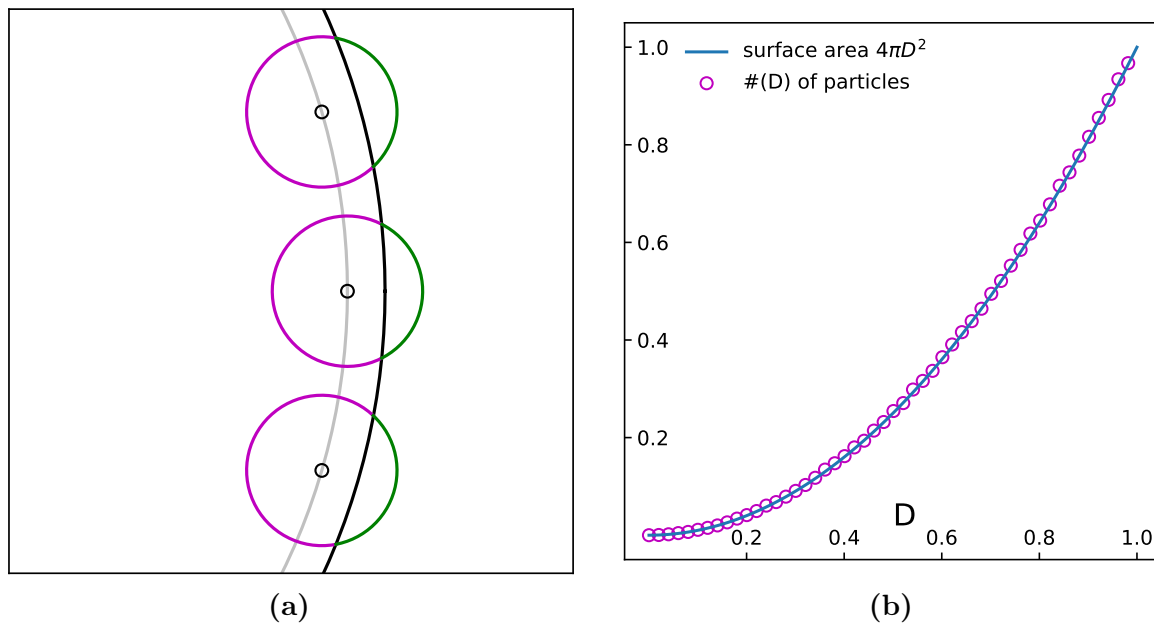
Figure 2.9: (a) Three particles inside a spherical confinement. Given the same pair-distance r and the fact that they all lie on sphere S_D, the reduction in the possible number of sampled pair-distances will be equal for all three particles. (b) For ideal gas particles confined inside a spherical confinement, the possible number of particles that can be found on the sphere S_D should be proportional with its surface area, $A_D = 4\pi D^2$. This is observed to be the case as the normalized experimental number of particles as a function of D matches the normalized S_D surface area. The experimental data is obtained by scattering 200 particles 50000 times in a confinement radius of $R = 1$.

Now, the objective is to obtain the total sum of the reduced surface area for the confined particles at a pair-distance r. By dividing the total sum with the sum of the "complete" surface area for all particles, the spherical ideal gas RDF can be obtained. This should in theory be equivalent to using the RDF algorithm to count pair-distances for spherically confined ideal gas particles if the reduced surface area - pair-distance assumption is true.

Considering Cartesian space where sphere S_R lie at $x, y, z = (0, 0, 0)$ and sphere S_r lie at $x, y, z = (D, 0, 0)$ such that

$$x^2 + y^2 + z^2 = R^2 \qquad \text{and} \qquad (x - D)^2 + y^2 + z^2 = r^2 \qquad (2.48)$$

Given that the two spheres intersect, x_i can be defined as the x-axis value of the sphere-sphere intersection

$$x_i = \frac{R^2 + D^2 - r^2}{2D} \qquad (2.49)$$

x_i also denotes the distance from $x = 0$ to an orthogonal yz plane that intersects sphere S_r to create a spherical cap with height h_c of size $0 \leq h_c \leq 2r$. h_c can be defined as

$$h_c = D + r - x_i = \frac{(D + r - R)(D + r + R)}{2D} \qquad (2.50)$$

x_i and h_c are illustrated in Figure 2.7b. By using the formulas for the spherical surface area A_r and spherical cap $A_{r,\text{cap}}$ for sphere S_r, the reduced surface area $A_{r,\text{red}}$ becomes

$$A_r = 4\pi r^2 \qquad A_{r,\text{cap}} = 2\pi r h_c \qquad A_{r,\text{red}} = 2\pi r (2r - h_c) = \frac{\pi r \left(R^2 - (D - r)^2\right)}{D} \qquad (2.51)$$

Criteria for overlap has to be defined as the spheres r and R only overlap for certain values of r and D. Two types of overlap occurs depending on the r value: when $r < R$ and when $r > R$. No overlap occurs occurs when $r < R$ and sphere r is completely immersed in sphere R. In that case, the total surface area of sphere r remains complete. No overlap occurs when $r > R$ and sphere R is completely immersed in sphere r. In that case the total surface area of sphere r is reduced to zero. Overlap occurs otherwise. The function for the surface of sphere r is given by r, D and R as $A_r(r < R, D, R)$ and $A_r(r > R, D, R)$

$$A_{r,\text{red}}(r < R, D, R) = \begin{cases} 4\pi r^2 & \text{for } r + D < R \\ \pi r \left(R^2 - (D - r)^2\right)/D & \text{for } r + D > R \end{cases} \qquad (2.52)$$

$$A_{r,\text{red}}(r > R, D, R) = \begin{cases} 0 & \text{for } R + D < r \\ \pi r \left(R^2 - (D - r)^2\right)/D & \text{for } R + D > r \end{cases} \qquad (2.53)$$

Now assume that the particles in the sphere S_R are distributed on n evenly spaced concentric circles with the sphere S_R center and a radius D that goes from 0 to R with a spacing $\Delta_D = R/n$ such that $D \in \{D_0 = 0, \ldots, D_{i-1}, D_i, D_{i+1}, \ldots, D_n = R\}$. By assuming that the number of particles that lie on the surface of sphere S_{D_i} is proportional

with its surface area $4\pi D_i^2$, the total sum of the "reduced surface area" for all the particles in the confinement at a pair-distance r can be obtained by summing the product of $A_{\mathrm{r,red}}$ and the surface area of sphere S_{D_i} for all D_i. By also dividing with the product of the complete sphere S_r surface area, $A_r = 4\pi r^2$ and sphere S_{d_i} surface area for all D_i, the analytical sphere RDF $g_0\left(r, < R, R\right)$ can be obtained. Since $A_{\mathrm{r,red}}$ consists of two functions, the case of $r < R$ will be used first.

$$g_o\left(r < R, R\right) = \frac{\sum\limits_{i=0}^{i=n} A_{\mathrm{r,red}}\left(r < R, D_i, R\right) 4\pi D_i^2}{\sum\limits_{i=0}^{i=n} 16\pi^2 D_i^2 r^2} \tag{2.54}$$

Expanding $A_r(r < R, D, R)$ into two sums

$$g_o\left(r < R, R\right) = \frac{\sum\limits_{i=0}^{i:D_i=R-r} 16\pi^2 D_i^2 r^2 + \sum\limits_{i:D_i=R-r}^{i=n} 8\pi^2 D_i^2 r(2r - h)}{\sum\limits_{i=0}^{i=n} 16\pi^2 D_i^2 r^2} \tag{2.55}$$

If the numerator and denominator are multiplied with Δ_D and $n \to \infty$, then the finite sums can be recognized as Riemann sums

$$\lim_{n\to\infty} \sum_{i=1}^{n} \Delta x \cdot f\left(x_i\right) = \int_a^b f(x)\mathrm{d}x \tag{2.56}$$

such that

$$g_o\left(r < R, R\right) = \frac{\lim_{n\to\infty} \sum\limits_{i=0}^{i:D_i=R-r} 16\pi^2 D_i^2 r^2 \Delta_D + \lim_{n\to\infty} \sum\limits_{i:D_i=R-r}^{i=n} 8\pi^2 D_i^2 r(2r - h)\Delta_D}{\lim_{n\to\infty} \sum\limits_{i=0}^{i=n} 16\pi^2 D_i^2 r^2 \Delta_D} \tag{2.57}$$

Applying Equation 2.56 to Equation 2.57 and integrating

$$g_o\left(r < R, R\right) = \frac{\int_0^{R-r} 16\pi^2 D_i^2 r^2 \mathrm{d}D + \int_{R-r}^{R} 8\pi^2 D_i^2 r(2r - h)\mathrm{d}D}{\int_0^{R} 16\pi^2 D_i^2 r^2 \mathrm{d}D} = \frac{16\,R^3 - 12\,R^2 r + r^3}{16R^3} \tag{2.58}$$

The same equation is obtained for $g_0\left(r > R\right)$ such that the analytical spherical RDF becomes

$$g_o\left(r, R\right) = \frac{16\,R^3 - 12\,R^2 r + r^3}{16R^3} \tag{2.59}$$

For $R = 1$, the RDF becomes

$$g_\text{o}\left(r\right) = \frac{1}{16}r^3 - \frac{3}{4}r + 1 \tag{2.60}$$

The accuracy of the analytical $g_o\left(r\right)$ can be tested with a comparison to experimental data. The two following methods have been used in this report

1. A simulated non-periodic RDF can be obtained by scattering ideal gas particles in a spherical confinement. This RDF has been obtained by scattering 500 particles 40000 times in a spherical confinement of R = 1.

2. PHS can be simulated in a spherical region of radius $R = 5\sigma$ with LJ walls of 10ϵ and 0.01σ cutoff. To reduce the structure effect, 55 PHS particles with a small diameter of $d_\text{PHS} = 0.5\sigma$ have been simulated, such that $\rho^* = 0.1$. 40000 configurations have been sampled.

After simulating case 1) in Python and 2) in LAMMPS, their respective RDFs are obtained from a standard RDF algorithm without periodicity (the non-periodic RDF algorithm is explained in Section 3.3). The RDFs are plotted against $g_o\left(r\right)$ using Equation 2.59
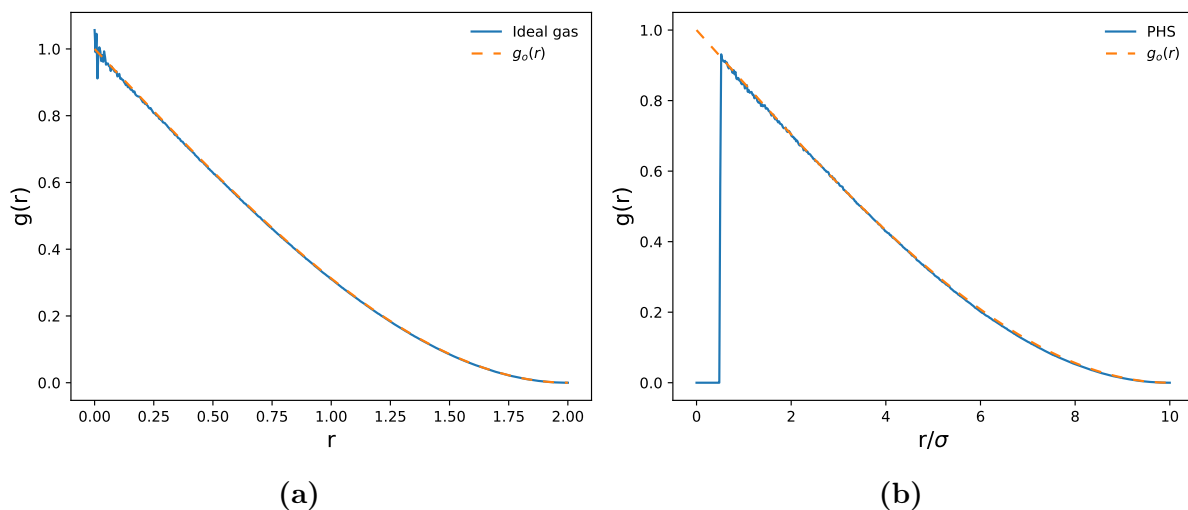
Figure 2.10: (a) The comparison between $g_0(r, R)$ and the spherically confined ideal gas RDF with confinement radius $R = 1$. (b) The comparison between $g_0(r, R)$ and the small PHS RDF at $\rho^* = 0.1$ and $d_\text{HS} = 0.5\sigma$ with confinement radius of $R = 5\sigma$.

As can be observed from the Figures 2.10a and 2.10b, the experimental data fits very well with the analytical $g_0\left(r, R\right)$ expression. The scatter at low r for the experimental ideal gas RDF in Figure 2.10a can be attributed to insufficient statistics, as sampling is more sensitive at low distances. The region in which the experimental PHS RDF equals zero in Figure 2.10b is caused by the particle volume. Because both the PHS density and

diameter is of low magnitude, the fluid will experience limited structural effect, and will as a result behave similarly to ideal gas particles with volume. Thus, Figure 2.10b is an excellent example of the pure non-periodicity effect on the PHS RDF calculation under non-periodic conditions.

Given that the radius R of the confinement sphere S_R tends to a large value or infinity, $g_0\left(r, R\right)$ will tend toward 1 at a relatively low pair-distance r, as seen in Figure 2.11.
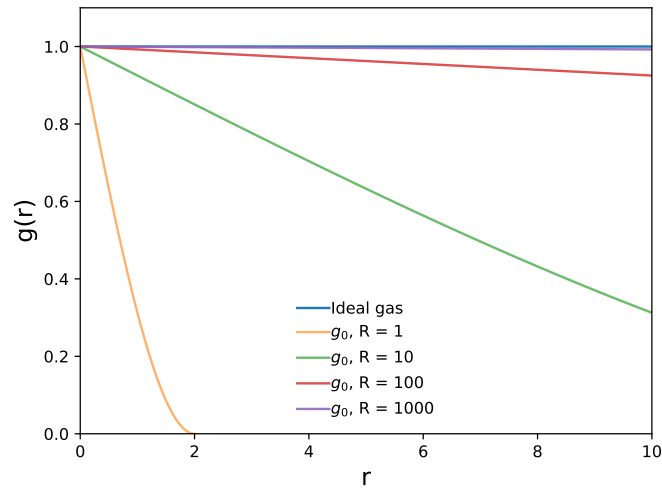
Figure 2.11: The comparison between the bulk ideal gas RDF and $g_0(r, R)$ for various confinement radii $R = 1, 10, 100$ and 1000.

When $R \to \infty$, the limit of the function $g_0\left(r, R\right)$ would equal 1 for any finite pair-distance r

$$\lim_{R \to \infty} g_0\left(r, R\right) = \lim_{R \to \infty} \left(1 - \frac{3r}{4R} + \frac{r^3}{16R^3}\right) = 1 \qquad \text{for} \qquad |r| < \infty \qquad (2.61)$$

showing that the spherical ideal gas RDF for a bulk spherical system $(R \to \infty)$ becomes equal to the bulk ideal gas RDF, which is always equal 1 independent of the pair-distance r.

3   Thermodynamic Methods

The simulation work in this thesis has consisted of performing MD simulations in LAMMPS [14]. For properties that are not directly obtainable from molecular simulations, the programming languages Fortran and Python have been used to implement thermodynamic theory to post-process data. Examples of post-processed properties include the spherical, non-periodic RDF and the first order perturbation term $a_{1,\mathrm{RDF}}$ that can be obtained by integrating the RDF using Equation 2.36. The LAMMPS, Fortran and Python scripts are found in the Appendix sections A1, A2 and A3. This section will therefore 1) detail the simulation conditions for the experiments performed LAMMPS and 2) explain the thermodynamic methods that are implemented in Python and Fortran.

An illustration of the simulation setup is shown in Figure 3.1, where particles are simulated inside a spherical confinement with a "hard" WCA wall potential $u_{\mathrm{WCA}}(r)$ as defined in Equation 2.30. There currently does not exist an option to purely have reflective walls for spherical geometries in LAMMPS. The automatically calculated volume for the system in LAMMPS is of the cubic simulation domain, which is different to the spherical confinement volume. As a result, properties such as pressure can still be natively calculated in LAMMPS, but have to be calculated in an alternative way as mentioned in the next section.
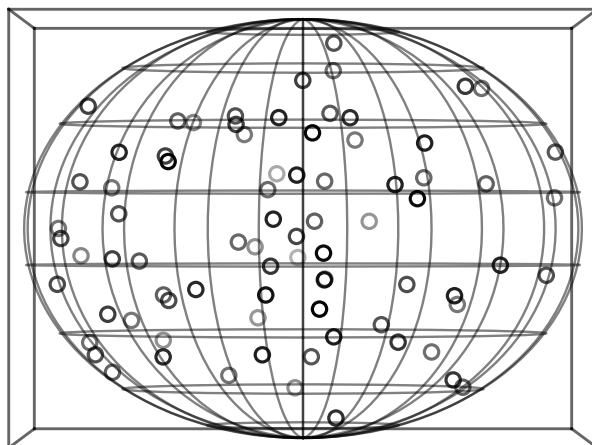
Figure 3.1: An illustration of the simulation setup in LAMMPS. Given a cubic simulation domain, a spherical region can be drawn up to exert a WCA wall potential, forcing the particles to stay inside the spherical confinement. Due to non-periodic boundary conditions being applied, no particles will exist outside the spherical confinement.

3.1   Simulation Conditions

The MD simulations in LAMMPS are performed in the NVT ensemble by using the Verlet algorithm for integrating the equations for motion and the Nose-Hoover thermostat for keeping a constant system temperature. With the exception of verifying bulk properties with theoretical data, all the fluids studied in this thesis are confined in spherical regions without periodic boundary conditions. To create a spherical confinement inside the simulation domain in LAMMPS, the FIX/WALL region command [24] is applied to create a spherical shell of a specified radius that exerts a WCA potential towards any particle that attempts to pass through the shell. To make the wall as hard as possible, the WCA wall potential is set to only exert strong repulsion by cutting and shifting the potential at its well bottom at a pair-wall distance of 0.01σ, with a strength parameter of 3ϵ, as seen in Equation 2.30.

The two fluids simulated in this thesis are the PHS and LJ/s fluids. Simulating the non-default LJ/s fluid is possible in LAMMPS by using a LJ/s add-on package [25]. Except for a difference in their characteristic pair potentials, the simuation settings, confinement radius and density range are generally the same for both fluids. As the PHS can only be simulated at $T^* = 1.5$, the simulation temperature is set to equal $T^* = 1.5$ for all simulations. Given that the liquid-gas phase transition of the bulk LJ/s fluid lie between $\rho^* = 0 - 0.85$ [20], the density range $\rho^* = 0.15 - 0.85$ is investigated in this thesis. The investigated confinement radius values are $R/\sigma = 5, 7.5, 10, 12.5, 15$.

In the stage of obtaining an initial configuration, all particles are randomly scattered in a region smaller than the investigated spherical region of radius R. The randomized distribution of particles are then moved by minimizing the total potential energy of the system. Then the initialization simulation is run with a time step of $\Delta t = 0.0001 - 0.0003$ for $10 \cdot 10^6$ total number of time steps. The production simulations are then run with a time step of $\Delta t = 0.0001 - 0.0003$ for $10\text{-}1000 \cdot 10^6$ total number of time steps, and is divided into 5 blocks when computation of standard deviations becomes necessary. The specific value for the time step and production run length depends on what kind of simulations that has been run. Generally a lower density simulation requires more samplings than higher density simulations. For sample scripts, refer to Appendix A1.

The fluid pressure and the first order perturbation term $a_{1,\text{AVG}}$ are directly calculated in LAMMPS. As mentioned previously, the intrinsic pressure calculation in LAMMPS uses

the volume of the simulation domain, which is different than the spherical confinement volume. The fluid pressure is therefore calculated by taking the average of the diagonal components of the per-atom stress tensor, divided by the product of the dimension and sphere volume, as explained in the COMPUTE STRESS/ATOM command [26]. The first order perturbation term $a_{1,\text{AVG}}$ is calculated by taking the ensemble average of the perturbative potential energy, as defined in Equation 2.42. To do so, $a_{1,\text{AVG}}$ is obtained by using the RERUN command on the dump file from the production run of the PHS fluid, where the pair potential is changed to a tabulated list of values describing the attractive region of the LJ/s pair-potential.

3.2 Thermodynamic Pressure

For a fluid constrained to the NVT ensemble, any property of the fluid can be obtained if an accurate expression for its reduced Helmholtz energy a_{fluid} exists. By neglecting the higher order terms, the BHPT LJ/s EOS to the first order can be expressed as

$$a_{\text{LJ/s}} \approx a_{\text{ID}} + a_{\text{HS}} + \beta a_1 \tag{3.1}$$

The expression can be differentiated with respect to V to obtain the LJ/s pressure [18]

$$P_{\text{LJ/s}} = -\left(\frac{\partial A_{\text{LJ/s}}}{\partial V}\right)_{T,N} = -Nk_BT\left(\frac{\partial a_{\text{LJ/s}}}{\partial V}\right)_{T,N} \tag{3.2}$$

By applying the $a_{\text{LJ/s}}$ expression into Equation 3.2, the LJ/s pressure can be expressed in the following way

$$P_{\text{LJ/s}} = \frac{Nk_BT}{V} - Nk_BT\frac{\partial a_{HS}}{\partial V} - N\frac{\partial a_1}{\partial V} \tag{3.3}$$

In reduced units

$$P_{\text{LJ/s}}^* = P_{\text{LJ/s}}\frac{\sigma^3}{\epsilon} = \rho^*T_* - N\sigma^3T_*\frac{\partial a_{HS}}{\partial V} + \frac{(\rho^*)^2}{\epsilon}\frac{\partial a_1}{\partial \rho^*} \tag{3.4}$$

where $T_* = Tk_B/\varepsilon$. The LJ/s pressure can also be rewritten as the sum of the HS pressure and the a_1 contribution

$$P_{\text{LJ/s}}^* = P_{\text{LJ/s}}\frac{\sigma^3}{\epsilon} = P_{\text{HS}}\frac{\sigma^3}{\epsilon} + \frac{(\rho^*)^2}{\epsilon}\frac{\partial a_1}{\partial \rho^*} \tag{3.5}$$

Given that only discrete values for a_1 exists from MD, discrete pressure values of $P_{\mathrm{LJ/s}}$ can be obtained by the use of central difference

$$\frac{\partial f(x)}{\partial x} \approx \frac{f(x+h) - f(x-h)}{2h} \tag{3.6}$$

3.3   RDF Algorithm

As can be observed from the subsection 2.7 and Figure 2.6, a key difference between bulk and nano fluids is the shape of their radial distribution functions due to the presence or absence of periodic boundary conditions. While there exists a number of methods to obtain bulk RDF through LAMMPS [27, 28], no such implementations exists for non-periodic fluids confined to non-cubic geometries. By "non-cubic", LAMMPS intrinsically calculates a system density using the volume of the cubic simulation domain, even if an additional constraint has been added to make the particles move in a smaller sphere. Luckily, by only omitting the periodicity requirement in the general bulk RDF scheme and using the correct fluid density, the scheme to produce small RDFs of any geometries is obtained. A general scheme to obtain a both a bulk and small RDF is presented here.

The principle is to construct a histogram $h(k)$ with n_k bins of size δr that counts accumulated pair-distances for n_c number of particle configurations. The algorithm of obtaining the RDF can then be explained in the following three steps

1. Calculate the pair separation $\mathbf{r}_{ij}$ for particles $\mathbf{r}_i$ and $\mathbf{r}_j$.

   - For periodic boundary conditions: If the pair-distance between $\mathbf{r}_i$ and a reflected particle $\mathbf{r}_j$ in another periodic cell is lower, then the pair distance $\mathbf{r}_{ij}$ is set to that value.

   - Otherwise: the pair-distance value $\mathbf{r}_{ij}$ stays the same.

   Increase the histogram count for the bin that $\mathbf{r}_{ij}$ falls into, $h(k) = h(k) + 1$

2. Repeat step 1 for all particles $1, \dots, N$ to obtain a complete histogram of pair separations, n_c times.

3. By considering a specific volume element, the radial distribution function is obtained through

$$g\left(k\mathrm{d}r + \frac{1}{2}\mathrm{d}r\right) = \frac{n(k)}{n^{\mathrm{ID}}(k)} \tag{3.7}$$

where the expression is an alternative form of Equation 2.19. $n(k)$ is the number of particles in bin k, defined in the following way

$$n(k) = \frac{h(k)}{Nn_{\mathrm{c}}} \qquad (3.8)$$

and $n^{\mathrm{ID}}(k)$ is the average number of ideal particles in the volume shell of thickness $k\delta r - (k-1)\,\delta r$

$$n^{\mathrm{ID}}(k) = \frac{4\pi\rho}{3}\left[(k\delta r)^3 - ((k-1)\,\delta r)^3\right] \qquad (3.9)$$

such that

$$g\left(r + \frac{1}{2}\delta r\right) = \frac{n(k)}{n^{\mathrm{ID}}(r)} = \frac{h(k)\,/\,(Nn_{\mathrm{c}})}{\frac{4\pi\rho}{3}\left[(r+\delta r)^3 - r^3\right]} \qquad (3.10)$$

Lists of equilibrium configurations in the form of dump files can be obtained by running simulation runs in LAMMPS. This thesis has applied this general non-periodic RDF algorithm (implemented in Fortran and shown in Appendix A2) on those dump files to obtain small RDFs from simulation. The RDFs calculated in this thesis uses $n_{\mathrm{c}} = 40000$ particle configurations and a spacing $\delta r = 1/50$.

4 Results and Discussion

A number of simulations have been performed in LAMMPS to investigate the PHS and LJ/s fluid behaviour under spherical confinement at the temperature of $T^* = 1.5$ with $d_{\mathrm{BH}}\left(T^* = 1.5\right) = 0.964239\sigma$. The data will therefore be used to map and extend the ability of the general BHPT to predict fluid behaviour under spherical confinement in this section. Since the thesis relies on the PHS fluid to accurately represent HS fluid behaviour, the first subsection will test this approximation by comparing HS fluid properties to simulation PHS fluid properties obtained from LAMMPS. The following subsections will then discuss the differences between bulk and small system fluids and how to apply the BH perturbation theory to fluids in small systems.

This chapter requires the use of the bulk HS RDF for $d_{\mathrm{BH}}\left(T^* = 1.5\right) = 0.964239\sigma$ at a large range of densities. The analytical representation of the Percus-Yevick (PY) bulk HS RDF derived by [1] is used in this thesis.

4.1 The HS and PHS fluid

The assumption that PHS replicates HS fluid behaviour at $T^* = 1.5$ can be tested by plotting the HS pressure obtained from the CS EOS with the pressure obtained from simulating PHS particles in a system with periodic boundary conditions. The HS and PHS pressures are shown to be indistinguishable in Figure 4.1
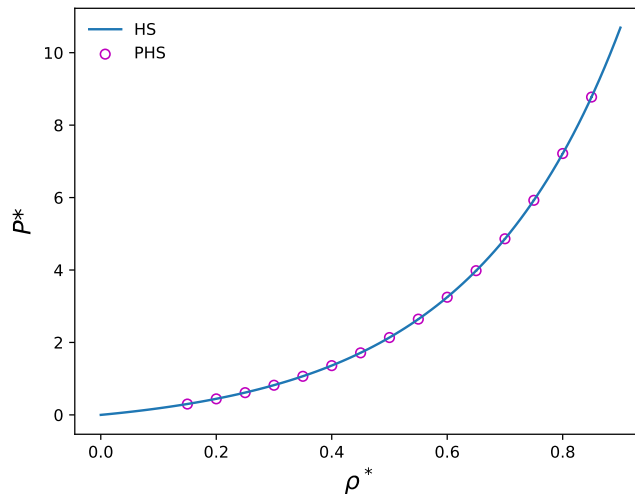
Figure 4.1: The bulk HS and PHS pressure as a function of the reduced density ρ^* at $T^* = 1.5$. The HS pressure is calculated from the CS EOS while the PHS pressure is obtained from LAMMPS simulation. The error is plotted as two standard deviations, however the error is so small it cannot be seen.

The HS RDF is another fluid property that is of importance in this thesis. The bulk HS RDF can be obtained from the analytical PY HS RDF expression while while the bulk PHS RDF can be calculated according to Subsection 3.3. The bulk HS and PHS RDF at $\rho^* = 0.85$ and $d_{HS} = 1\sigma$ is seen to be very similar in Figure 4.2a
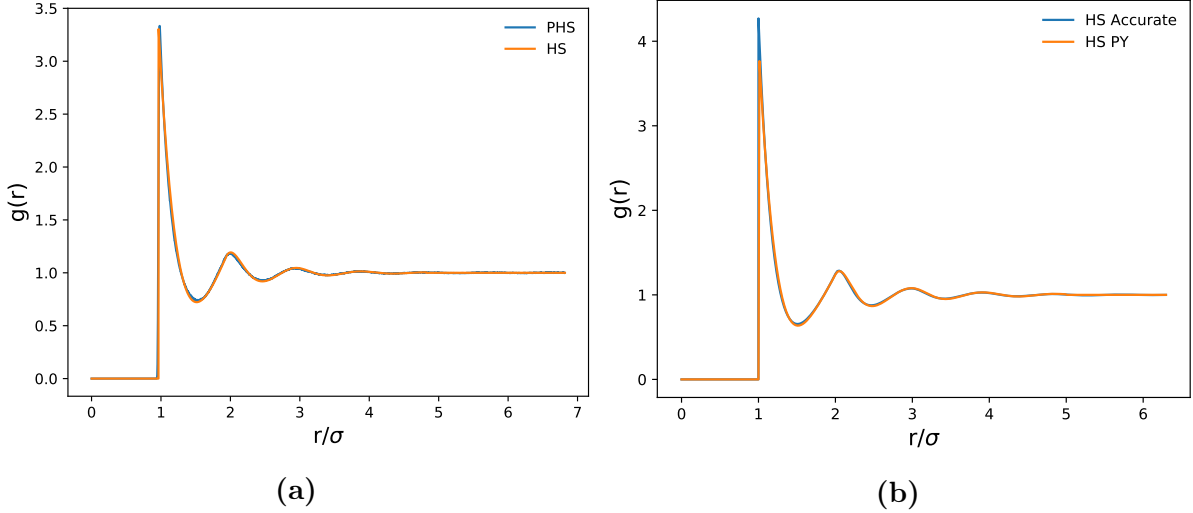
Figure 4.2: (a) Bulk PHS RDF is plotted together with the analytical PY HS RDF as a function of pair-distance r with $d_{HS} = d_{BH}$ ($T^* = 1.5$). The bulk PHS RDF is obtained from LAMMPS. (b) The analytical PY HS RDF is plotted together with a more accurate HS RDF from [2] with $d_{HS} = 1\sigma$.

Both the contact value $g\left(\sigma\right)$ and the general structural trend is observed to match well. However, the bulk PY HS RDF is known to underpredict the contact value [15], which means that the PHS RDF underpredicts the contact value as well. A comparison between the PY HS RDF and a more accurate HS RDF from [2] is plotted in Figure 4.2b, where a clear contact value difference can be observed. Given good statistics and sufficiently small histogram bins for the PHS RDF calculation, a possible cause for its underprediction can lie in how the PHS and HS potentials intrinsically produce different fluids behaviour. If the RDF contact value is ignored however, the general HS and PHS fluid structure can be seen as approximately equivalent. Therefore, the RDF contact value will not be discussed in the following sections, while the overall PHS fluid structure will be seen as an approximately accurate estimation of HS fluid structure.

4.2   Bulk and Small LJ/s Fluid Properties

The next step forward is to compare the properties of bulk and small LJ/s fluids. One of the preliminary results obtained from simulating small systems is the existence of a pressure difference between the bulk and nano LJ/s fluids, shown in Figure 4.3. The bulk LJ/s pressure is obtained from LAMMPS simulation, and can also be approximated from the LJ/s BHPT EOS to the first order using Equation 3.3. The difference between the two is caused by the negligence of higher order terms for the BHPT EOS of first order. The LJ/s small pressure is obtained in LAMMPS for confinement radius of $R = 5\sigma$. By taking basis in BHPT, the pressure difference can be caused by a change in the reference fluid behaviour and/or its fluid structure, which will in turn cause a deviation in the pressure contributions from a_{HS} and/or a_1.
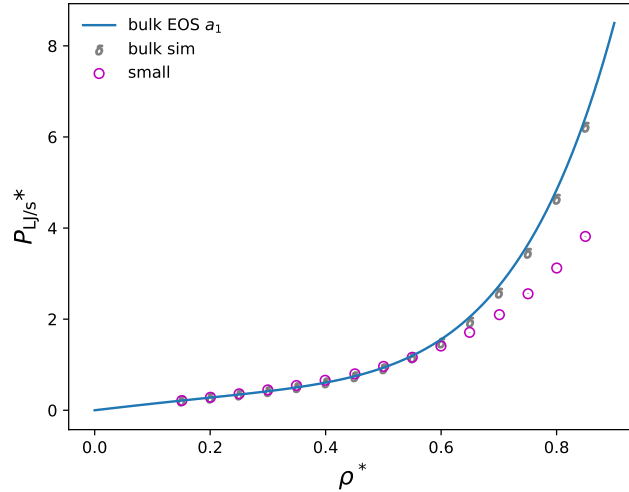
Figure 4.3: The bulk and small LJ/s pressure as a function of fluid density, at $T^* = 1.5$. The confinement radius is $R = 5\sigma$ for the small pressure. The bulk pressure is obtained from LAMMPS simulations SIM and the bulk BHPT EOS of first order a_1 while the small pressure is obtained from LAMMPS. The error is plotted as two standard deviations, but is so small it cannot be seen.

Out of the two possibilities a_{HS} and a_1, a_1 is readily observed to deviate from bulk to small systems as $a_{1,\mathrm{RDF}}$ relies on the reference system RDF. In comparison to a bulk system where the RDF tends towards 1 when $r \to \infty$, the RDF of a small system will tend towards zero as no particles outside the confinement will exist or interact with the particles inside the nano system. The difference between the small and bulk RDF is explained more in-depth in Section 2.7. By obtaining the small PHS RDF from LAMMPS, the bulk HS and small PHS RDF at $\rho^* = 0.15$ and $\rho^* = 0.85$ are shown in Figure 4.4.
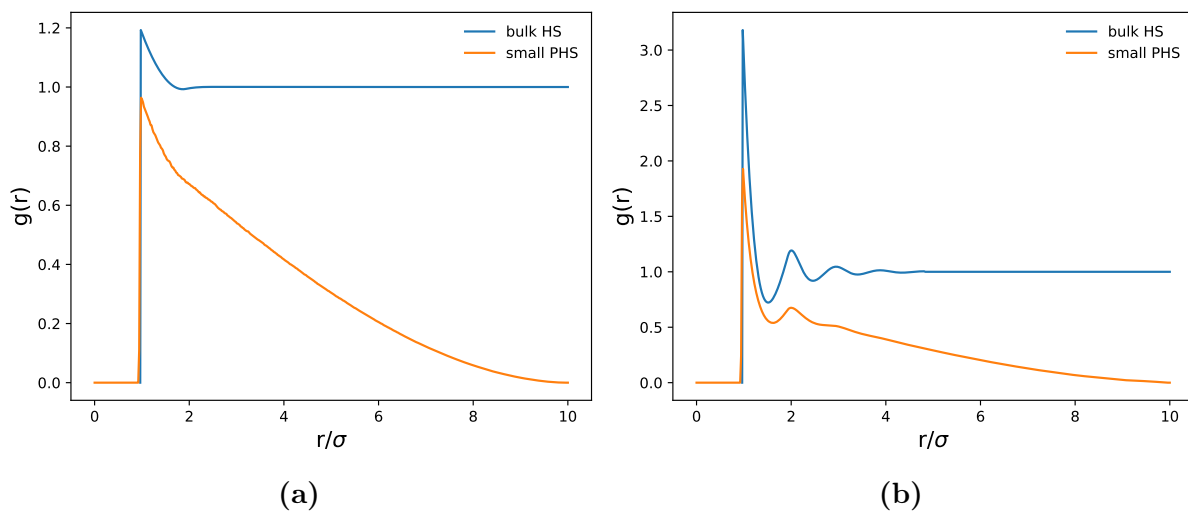
Figure 4.4: The bulk HS and small PHS RDF at (a) $\rho^* = 0.15$ and (b) $\rho^* = 0.85$. as a function of pair-distance r. The bulk HS RDF is obtained from the analytical PY HS RDF expression, while the small PHS RDF is obtained from LAMMPS simulations.

The stark difference between the bulk and small RDFs mark a clear departure from the general range of obtainable bulk a_1 values for small systems, as the RDF reduction will change the obtainable small $a_{1,\text{RDF}}$ values from integrating the RDF using Equation 2.36. By integrating the experimental small RDF using Equation 2.36 and using LAMMPS RERUN, discrete values of small $a_{1,\text{RDF}}$ and $a_{1,\text{AVG}}$ can be obtained at a range of densities, and is displayed in Figure 4.5 together with bulk a_1.
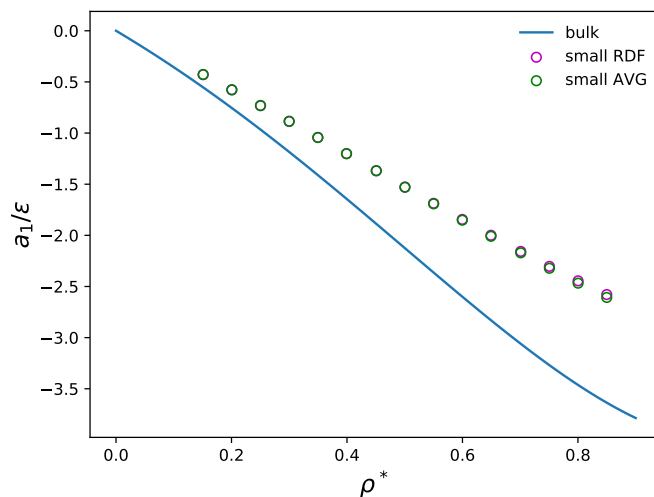
Figure 4.5: The bulk and small first order term a_1 from BHPT. The bulk a_1 is obtained from the BHPT LJ/s EOS, while the small RDF a_{RDF} is obtained from the small PHS RDF using Equation 2.36 and the small a_{AVG} is obtained from LAMMPS simulation. The error is plotted for a_{AVG} with two standard deviations, but is so small it cannot be seen.

The similarity between $a_{1,\text{RDF}}$ and $a_{1,\text{AVG}}$ shows that the small RDF can be a good descriptor of fluid structure in small systems. The deviation between the two at high

densities can be caused by a number of reasons, including numerical integration of Equation 2.36 to obtain $a_{1,\text{RDF}}$, insufficient sampling for the RDF and inaccurate tabulation of the LJ/s potential under RERUN to obtain $a_{1,\text{AVG}}$. The difference in the bulk and small a_1 values can be a plausible cause for the pressure difference in Figure 4.3. However, the reference system can also contribute to the pressure difference if the HS fluid is also dependent on smallness effects. From LAMMPS, a distinct bulk and small pressure difference is also observed for the reference system, shown in Figure 4.6a. Therefore, both a_{HS} and a_1 change under confinement. By using the experimental small PHS pressure and the pressure contribution from the small a_1 in Equation 3.5, the small LJ/s pressure can possibly be predicted. The resulting LJ/s pressure from a "small" BHPT EOS is shown in Figure 4.6b, with the use of the small PHS and small a_1 BHPT pressure contribution

(a)   (b)
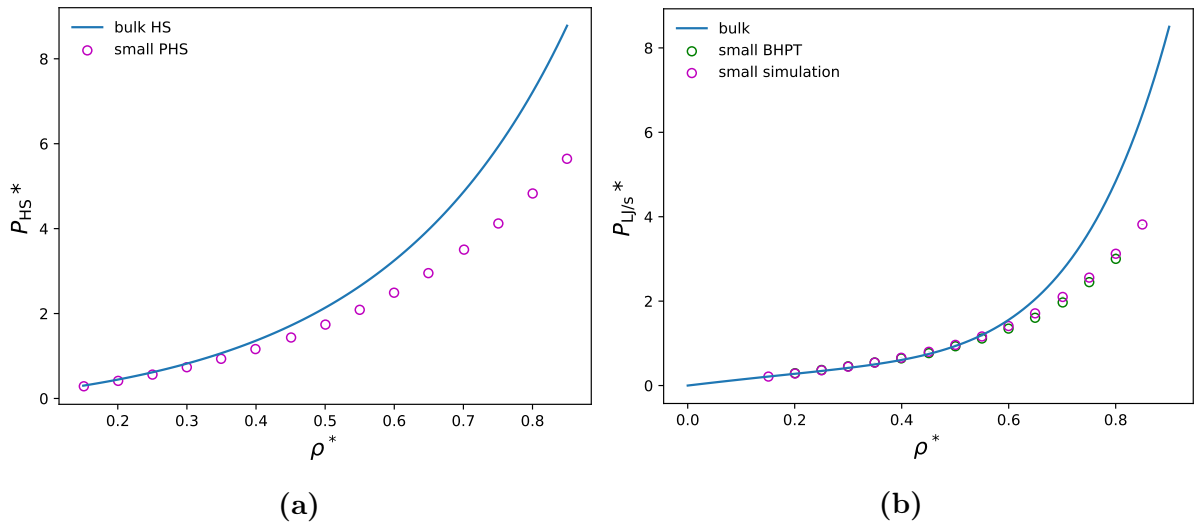
Figure 4.6: (a) Bulk HS and small PHS pressure at $T^* = 1.5$ and $R = 5\sigma$. (b) Bulk and small LJ/s pressure is plotted as a function of density. Bulk LJ/s pressure is obtained from BHPT of first order. The small $P_{\text{LJ/s}}*$ from "small simulation" is obtained using LAMMPS while "small BHPT" is obtained from BHPT using both small reference and a_1 pressure values at $R = 5\sigma$.

According to Figure 4.6b, the small BHPT EOS of first order is able to predict the experimental LJ/s pressure very well at a high temperature $T^* = 1.5$, although a certain deviation from the experimental LJ/s pressure can be seen at high reduced densities. The deviation between the simulated and predicted BHPT LJ/s pressure can possibly be attributed to be caused by numerical error such as insufficient simulation steps, numerical integration of a_1, numerical differentiation of a_1 and the exclusion of higher perturbation terms a_2, a_3 and so on. Based on the assumption that the difference is only caused by numerical errors, an accurate representation of a small LJ/s BHPT EOS can possibly be obtained by having a correct representation of a small HS EOS and small a_1 values. The

next steps forward is therefore to better understand the non-periodic RDF transformation
and how to possibly obtain a small HS EOS.

4.3   First Order Perturbation Term

As mentioned previously, the lack of periodic boundary conditions is one of the primary
factors for the small RDF trend, which in turn causes a difference between bulk and small
a_1 values. A question to ask here is if the bulk-small RDF difference is only caused by the
non-periodicity factor, in the sense that no other smallness factors influences the small
PHS RDF shape. For example, given that is the case and that the non-periodic factor
can be captured analytically, then the bulk HS RDF can theoretically be transformed
into a "small" bulk-transformed RDF (BT-RDF) that should accurately recapture small
a_1. If the BT-RDF does end up behaving similarly to small RDFs , then the spherical
confinement does not alter the fluid structure in a major way. Any deviation between the
BT and small RDF suggests that additional small factors play a role in altering the small
system fluid structure. Section 2.7 derives an analytical RDF g_0 for spherically confined
ideal gas describing the non-periodic reduction trend, and can be multiplied with bulk
RDFs to obtain BT-RDFs

$$g(r)_{\text{small}} = g(r)_{\text{bulk}} \times g_0 \qquad (4.1)$$

The product of bulk HS RDFs and g_0 is therefore plotted in Figure 4.7 together with
small RDFs at the same densities for the confinement radius $R = 5\sigma$.

Figure 4.7: The BT and small PHS RDF at (a) $\rho^* = 0.15$ and (b) $\rho^* = 0.85$ as a function
of pair-distance r, for the confinement radius $R = 5\sigma$. The BT RDF is obtained using
Equation 4.1 while the small PHS RDF is obtained from LAMMPS simulations.

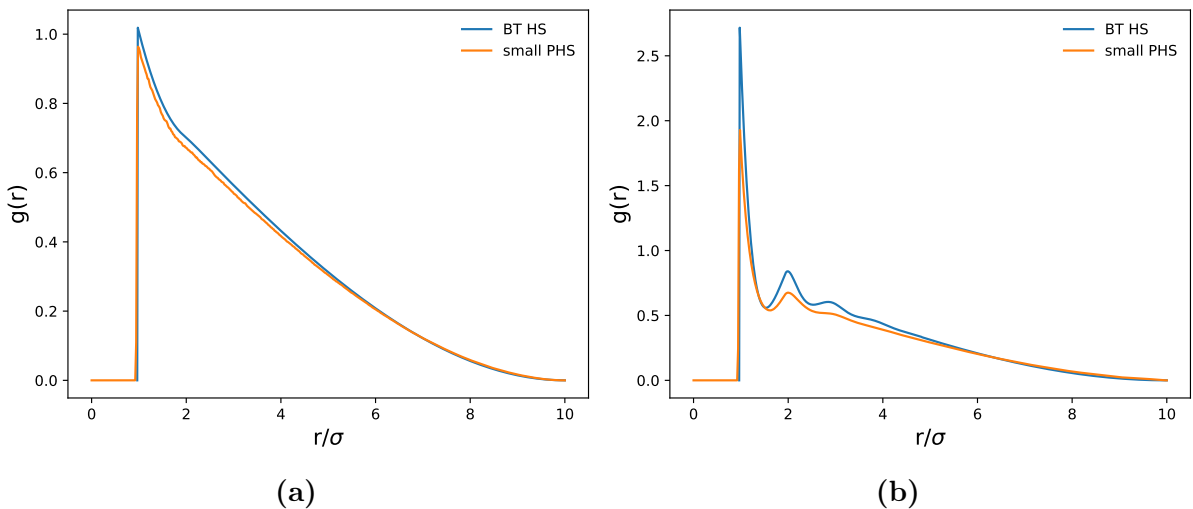By simply multiplying the bulk RDF with g_0, the BT-RDF at a low density of $\rho^* = 0.15$ is able to represent small RDFs very well. At the same time, the two RDFs becomes less similar at a higher density of $\rho^* = 0.85$, suggesting that the confined fluid exerts a more alternative structure than pure bulk structure. The BT-RDF is observed to exert sharper peaks in comparison to the more smoother small RDF peaks, while at the same time becoming indistinguishable after $r = 5\sigma$. The difference between the BT and small RDF can be mapped out by proposing an extra variable x_0 that depends on the pair-distance r and the confinement radius R at a certain reduced density ρ^*

$$g_{\text{bulk}}(r) \, g_0(r) \, x_0(r, R) = g_{\text{small}}(r) \tag{4.2}$$

such that

$$x_0(r, R) = \frac{g_{\text{small}}(r)}{g_{\text{bulk}}(r) \, g_0(r)} \tag{4.3}$$

In the low density case, x_0 should be close to unity as the non-periodicity becomes the primary smallness factor. With increased density, x_0 should deviate from unity to capture the additional small structure effect that occurs in the fluid system. The small-system density dependence that occurs can possibly be compared to the small-system dependence of the confinement radius R. At the same density ρ^*, x_0 should in theory tend towards unity as the confinement radius R tends towards infinity, since the small system fluid will tend towards bulk size. At low R, perhaps the small structure factor will deviate from unity due to any additional packing constraint enforced by the confinement wall. The variation of x_0 with system density ρ^* and confinement radius R is plotted in Figures 4.8 and 4.9

As can be seen in the Figures 4.8 and 4.9, x_0 tends towards unity with increasing R and decreasing ρ^*, suggesting that the periodicity factor becomes the main difference between bulk and small system fluids. When R decreases and ρ^* increases however, an additional smallness structure factor becomes prominent in the small system. Perhaps the more interesting trend is how the structure factor x_0 is dependent on the confinement radius R at a constant density of $\rho^* = 0.85$. While the density is kept at a constant, the structure factor becomes incrementally more prevalent with decreasing confinement radius R, suggesting that the decrease in R somehow disrupts the "bulk" structure in the confined fluid. One hypothesis is that the confinement wall "irregularly" constrain a certain volume that PHS particles can or cannot exist in, in comparison to bulk fluids
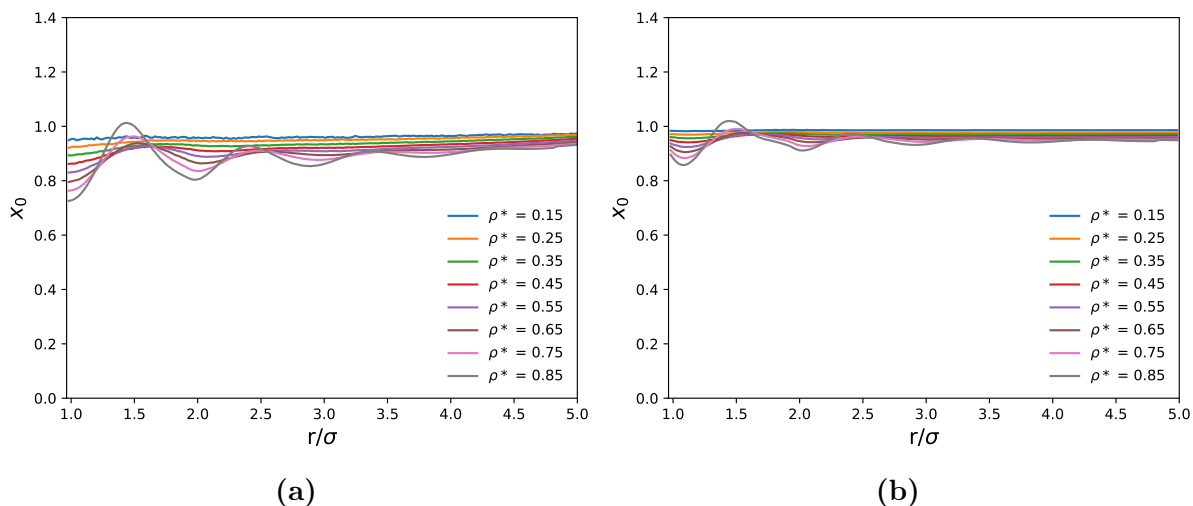
Figure 4.8: The density dependency of x_0 in Equation 4.3 at (a) $R = 5\sigma$ and (b) $R = 15\sigma$.
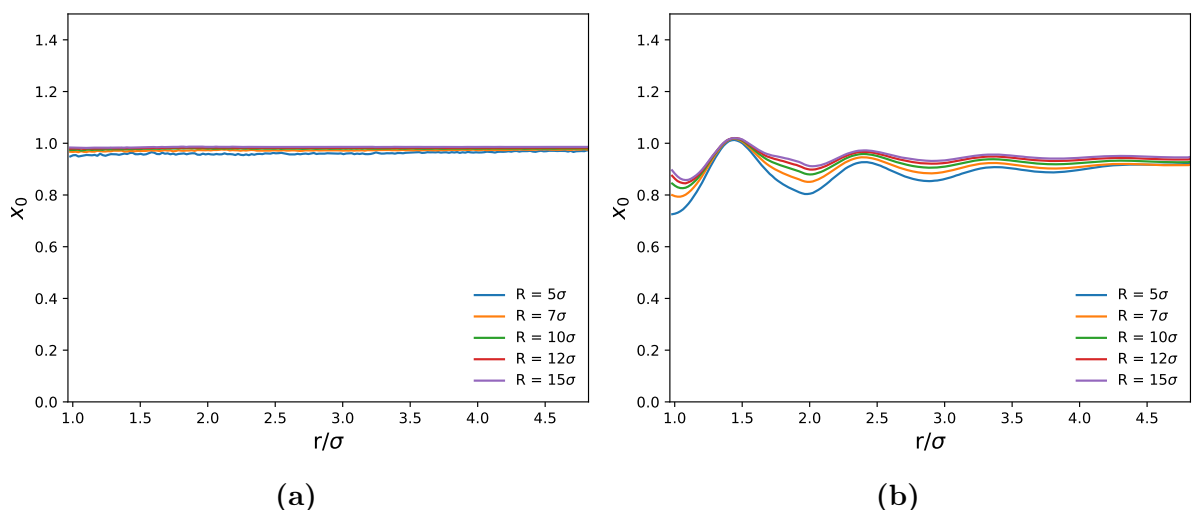
Figure 4.9: The R dependency of x_0 in Equation 4.3 at (a) $\rho^* = 0.15$ and (b) $\rho^* = 0.85$.

at the same density. Such a disruption advocates for the presence of a heterogeneous structure, where certain areas in the spherical confinement will have distinctly different densities.

4.3.1   Particle Adsorption

An interesting trend to observe is therefore the density variation from the sphere confinement center to its radius R. For bulk fluids, the density for a volume element anywhere within the fluid should on average always equal the bulk density. For fluids in small systems, the radial density variation from the confinement center is shown in Figure 4.10
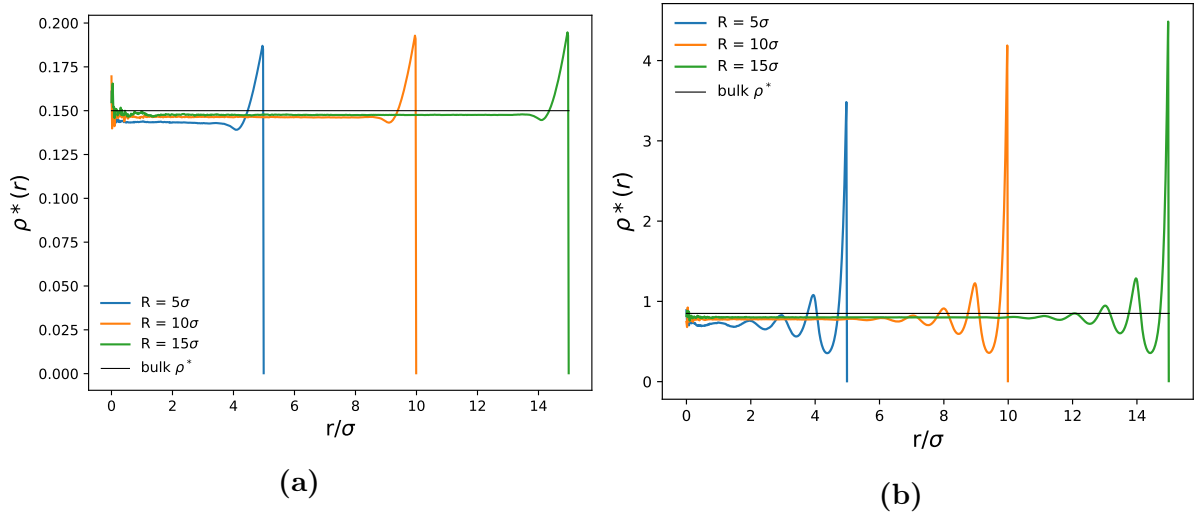
Figure 4.10: The density variation of the PHS fluid within confinements of $R = 5\sigma, 10\sigma$ and 15σ for (a) $\rho^* = 0.15$ and (b) $\rho^* = 0.85$. The data is obtained by iterating through simulation configurations using the Fortran program DENSITY_VARIATION in Appendix A2.

Fluids in small systems are observed to have a specific density arrangement that deviates from the fluid density close to the confinement wall. The density peak(s) suggests that particles are especially prone to concentrate there. An explanation can be that the confinement wall does not push particles in the same way particles do. For example, a particle in the center of the small system fluid will be pushed by particles in all directions, while particles pushed towards the wall will not be as pushed back into the fluid by the non-moving wall. As a result of the anisotropic particle pushing, particles close to the wall will be more prone to stay there.

As can also be seen in Figure 4.10, the shape and length of the density arrangement is very independent of the confinement size, with the exception that the magnitude slightly increases with R. The independence of the density arrangement length with R suggests that the density arrangement "shell" that encompass the "inner-core" (IC) of the fluid scales with the surface area of the confinement sphere. By increasing R, the fraction of the IC fluid structure will increase, which will in turn reduce the impact of the density arrangement at the surface. Another observation from Figure 4.10 is that the IC density is lower and will tend towards the overall fluid density with increasing R. The low IC density magnitude suggests that particles are depleted from the IC region to be adsorbed in the density arrangement region at the surface wall. Since the density arrangement region is predicted to scale with the confinement surface area, the number of adsorbed particles should do so too. With increasing R, the fraction of adsorbed particles will

therefore decrease in comparison to the fraction of the IC particles. The IC density can be obtained by integrating the linear region in the density variation observed in Figure 4.10,

$$\rho_{\text{IC}}^* = \frac{1}{(4/3)\pi r^3} \int_0^r \rho^* (r) \, 4\pi r^2 \mathrm{d}r \tag{4.4}$$

Finding the IC density can be difficult for confinements of low R however, as the distinction between the IC and outer-core (OC) adsorption region can be hard to define. This can especially be seen for the $R = 5\sigma$ and $\rho^* = 0.85$ case in Figure 4.10b, as the majority of the density region varies with r. For the $R = 10\sigma, 15\sigma$ cases at $\rho^* = 0.85$, a clear distinction can be made, where the linear density regions is qualitatively observed to stop at around $R - 5.5\sigma$. For all the cases at $\rho^* = 0.15$, the linear density region is observed to stop around $R - 2\sigma$. By neglecting the $R = 5\sigma$, $\rho^* = 0.85$ case, the IC and overall fluid densities are obtained and plotted in Figure 4.11
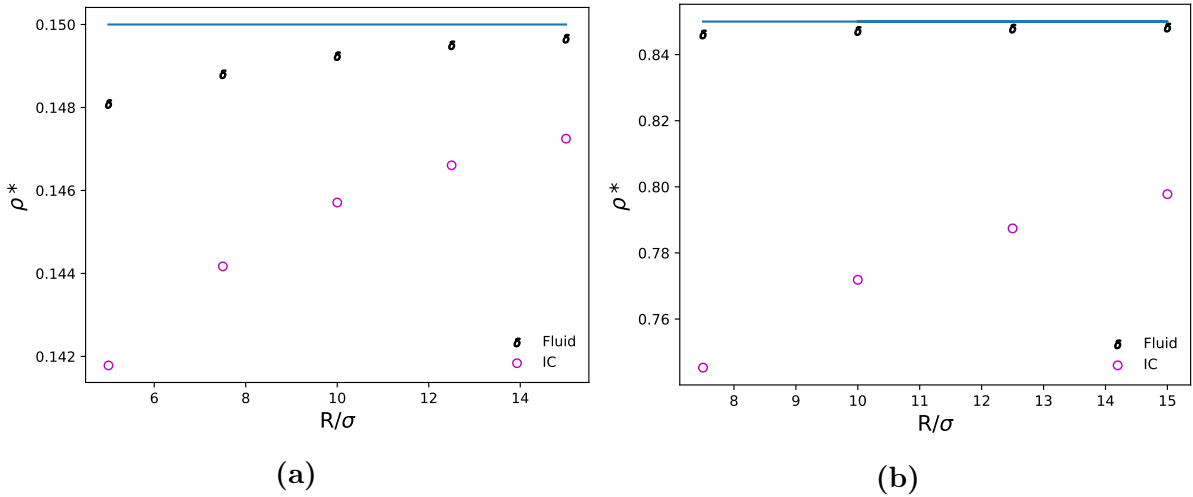
Figure 4.11: The PHS IC and fluid density for (a) $\rho^* = 0.15$ and (b) $\rho^* = 0.85$ as a function of R, calculated using Equation 4.4 on the density variation curves in Figure 4.10. The blue line shows the expected total fluid density of the system.

Both the IC and calculated fluid density is observed to tend towards the bulk density with increasing R. An explanation for the difference between the calculated and actual fluid density can be due to insufficient sampling of the density variation in Figure 4.10. Given the IC density, the adsorption per surface area Γ can be obtained in the following way

$$\Gamma = \frac{1}{4\pi R^2} \int_0^R 4\pi r^2 \left(\rho^* (r) - \rho_{\text{IC}}^* \right) \mathrm{d}r \tag{4.5}$$

Γ is plotted in Figure 4.12, and is observed to be relatively proportional with confinement surface area. The small difference between the adsorption values can be caused by

insufficient sampling and the various ways particles with diameter d_{BH} ($T^* = 1.5$) can be stacked close to the surface area at different R.

(a)   (b)
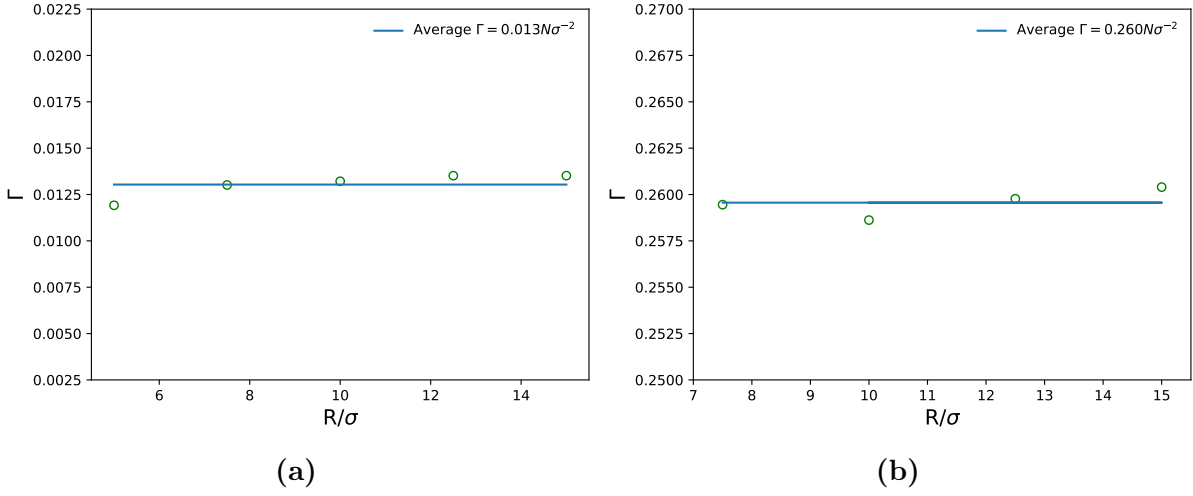
Figure 4.12: The adsorption Γ at (a) $\rho^* = 0.15$ and (b) $\rho^* = 0.85$ as a function of R, using Equation 4.5. The average adsorption is plotted alongside.

The average Γ for $\rho^* = 0.15$ and 0.85 is displayed with with two standard deviations

$$\Gamma\left(\rho^* = 0.15\right) = 0.013 \pm 0.001 N\sigma^{-2} \qquad \Gamma\left(\rho^* = 0.85\right) = 0.260 \pm 0.001 N\sigma^{-2} \qquad (4.6)$$

By multiplying the average surface adsorption with the surface area of confinement sphere R, the IC core of any R can be predicted

$$\rho^*_{\text{IC}} = \frac{(4/3)\pi R^3 \rho^* - 4\pi R^2 \Gamma}{(4/3)\pi R^3} \qquad (4.7)$$

The predictive and experimental IC densities are plotted together in Figure 4.13, and is observed to match very well. Given the adsorption value for a certain fluid density, the IC density can be predicted for spherical confinements of any R of relative size. A "relative sized" R is defined as a confinement geometry of large enough R to create a distinct IC and OC separation. For example, Equation 4.7 will begin to predict nonphysical and negative IC densities at low R. If a "small" BHPT EOS require a clear distinction between IC and OC regions for fluids in small systems to work, then the case of $R = 5\sigma$ at $\rho^* = 0.85$ would prove to be a limit of its applicability.
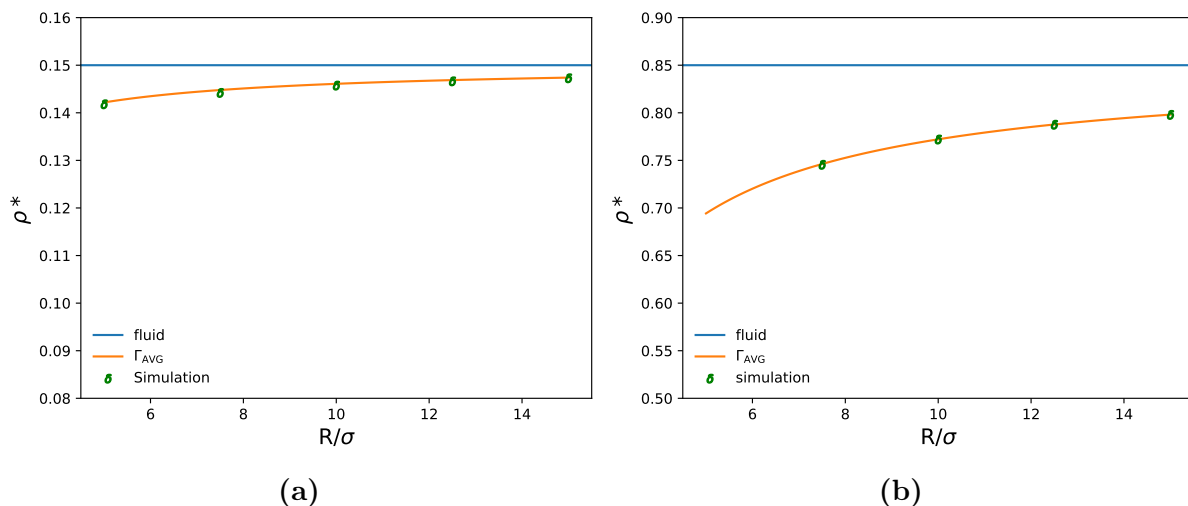
Figure 4.13: The simulated and predicted IC densies are plotted for (a) $\rho^* = 0.15$ and (b) $\rho^* = 0.85$ as a function of R. The predicted IC density is obtained from Equation 4.7. The blue line shows the expected total fluid density of the system.

4.3.2   Fluid Density Variation

A similar analysis can be performed on the density arrangement profile as a function of fluid density. Due to the intrinsic uncertainties that low confinement radii R have on the IC-OC structure separation, this fluid density dependency analysis will focus on the specific case of $R = 10\sigma$. By holding $R = 10\sigma$ constant and estimating the IC region to be between $r = 0$ and $R - 5.5\sigma$ for all fluid densities, the fluid density dependency on the density arrangement region and the IC density is shown in Figure 4.14
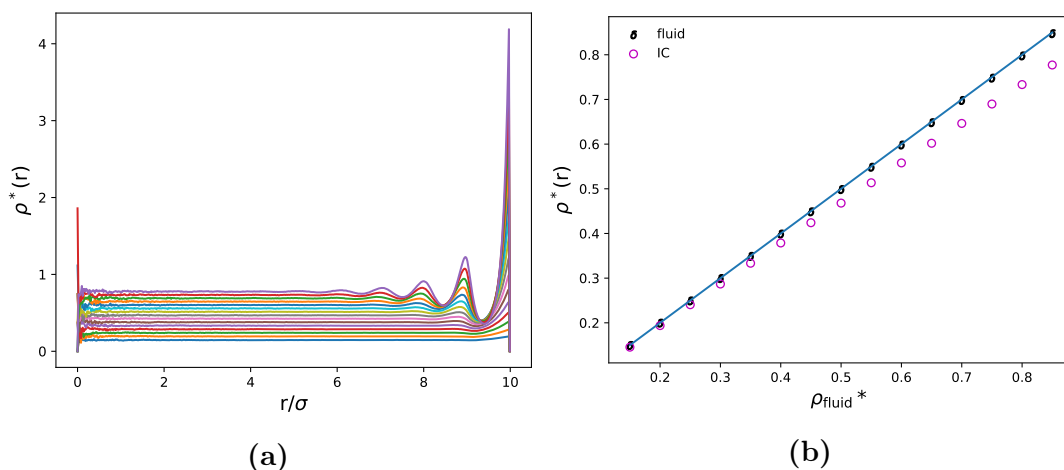
Figure 4.14: (a) The density variation within a spherical confinement of $R = 10\sigma$ for fluid densities of $\rho^* = 0.15 - 0.85$. The higher the fluid density is, the higher density variation profile it has. (b) The IC and fluid density for a spherical confinement of spherical confinement of $R = 10\sigma$, calculated using Equation 4.4 on the density variation equation curves in Figure 4.14a. The blue line shows the expected total fluid density of the system.

In comparison to how independent the density arrangement length is with R, the density arrangement region increases in size and structure variation with increasing fluid density. A consequence of the fluid density dependence is that more particles will be adsorbed on the confinement surface, which in turn will increase the IC density reduction. The significance of the distinct inner and outer core regions in relatively large confined fluids is that the majority of the fluid is composed of the inner-core region. As a consequence, confined fluids will more likely exert properties similar to bulk fluids of the inner-core density in comparison to the actual fluid density. Given that is the case, then a more accurate BT-RDF transformation can be obtained by using the IC density for the bulk RDF instead of the total fluid density. Such a transformation avoids the direct and possibly complicated consideration of the surface density arrangement region. More formally stated, the BT-RDF transformation can be improved from

$$g\left(\rho^* = \rho^*, r\right)_{\text{small}} = g\left(\rho^* = \rho^*, r\right)_{\text{bulk}} \times g_0 \tag{4.8}$$

to

$$g\left(\rho^* = \rho^*, r\right)_{\text{small}} = g\left(\rho^* = \rho^*_{\text{IC}}, r\right)_{\text{bulk}} \times g_0 \tag{4.9}$$

By using the experimental IC densities displayed in Figure 4.14b, the modified bulk RDF transformation is shown in Figure 4.15

Figure 4.15: The comparison between the small PHS RDF obtained from LAMMPS and the BT HS RDF from Equation 4.9 for (a) $\rho^* = 0.15$ and (b) $\rho^* = 0.85$ at a confinement radius of $R = 10\sigma$.

The overall trend between the BT-RDF and small RDF is observed to significantly improve, but the BT-RDF is somehow vertically shifted by a constant value. This non-unity shift can

also be observed in the low density and high R case of x_0 (Figure 4.9a), where the constant multiplication factor is seen to tend towards unity with increasing R. One possibility is that the vertical shift is caused by the adsorption effect. For example, the small RDF algorithm does not discriminate between the inner and outer core densities, but divides the pair-distance histogram with the total fluid density. As a result of the IC particle depletion, the relative probability of finding a particle inside the small system fluid would likely decrease in comparison to the ideal gas distribution. In other words, the small $n(k)$ will reflect the histogram of an IC density fluid while the $n^{\mathrm{ID}}(k)$ will reflect the histogram of an ideal gas with the actual fluid density in the RDF Equation $g(r) = n(k)/n^{\mathrm{ID}}(k)$ (Equation 3.7) where $\rho_{\mathrm{IC}}^* < \rho^*$, such that the numerator and denominator histograms reflects fluids of two different densities. This probability decrease is not seen in the BT-RDF, as both the $n(k)$ and $n^{\mathrm{ID}}(k)$ reflect fluids of the same density ρ_{IC}^*. By simply multiplying the BT with the density fraction $(\rho_{\mathrm{IC}}^*)/\rho^*$, the $n^{\mathrm{ID}}(k)$ will reflect the histogram of an ideal gas with the actual fluid density ρ^* while the $n(k)$ will still reflect the histogram for a fluid with IC density. Therefore, one can perhaps obtain a more matching RDF transformation by using the normalization factor $(\rho_{\mathrm{IC}}^*)/\rho^*$

$$g\left(\rho^* = \rho^*, r\right)_{\mathrm{small}} = g\left(\rho^* = \rho_{\mathrm{IC}}^*, r\right)_{\mathrm{bulk}} \times g_0 \times \frac{\rho_{\mathrm{IC}}^*}{\rho^*} \tag{4.10}$$

The BT-RDF transformation using Equation 4.10 is shown in Figure 4.16
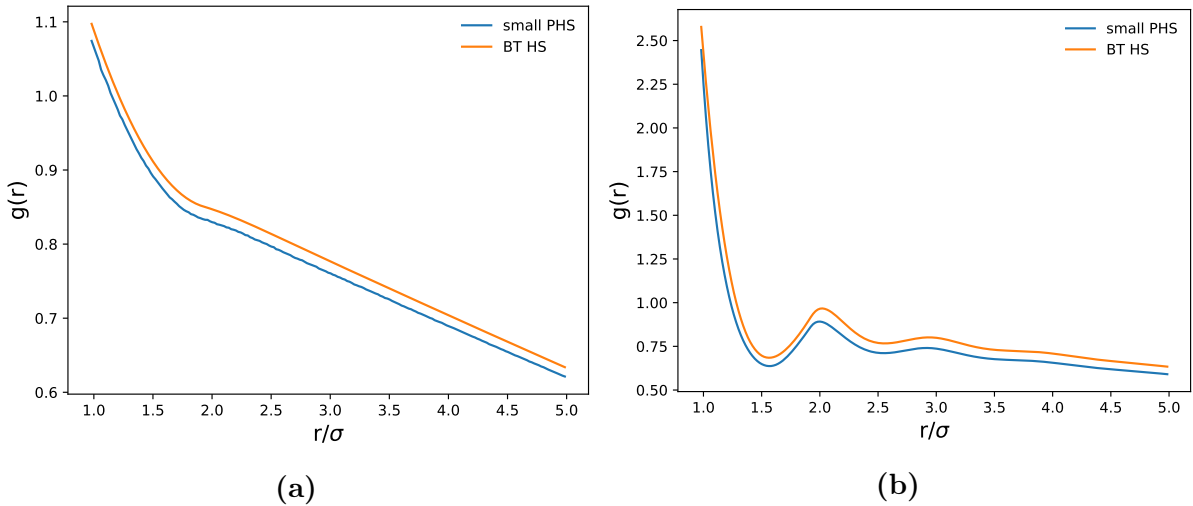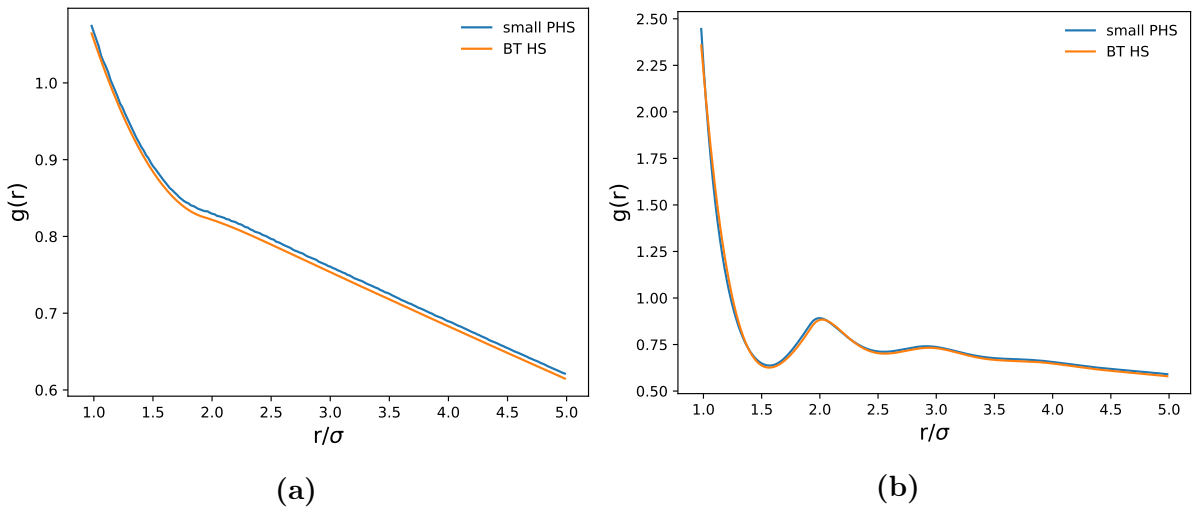

Figure 4.16: The comparison between the small PHS RDF obtained from LAMMPS and the final BT HS RDF from Equation 4.10 for (a) $\rho^* = 0.15$ and (b) $\rho^* = 0.85$ at a confinement radius of $R = 10\sigma$.

An alternative method to obtain a similar result would be to find the number of particles that can be obtained from integrating the small RDF, as it should in theory equal the

number of particles that can be obtained from the BT-RDF. However, given that the IC density trend is known, this method would require the additional information of knowing the experimental small RDF.

Figure 4.16 shows excellent match between the two RDFs, proving the RDF transformation using Equation 4.10 to be working well. At this point, the relative error between the two RDFs can be caused by a number of reasons, including additional smallness effects, the density arrangement region, that PHS RDFs are being used instead of HS RDFs and insufficient sampling for the RDF and inner-core density calculation. The good match also suggests that the density variation region does not modify the HS RDF in any other major way than just to adsorb particles to the wall. Without a further investigation of these factors, the BT a_1 is calculated and plotted together with the small a_1 in Figure 4.17. The two a_1 match exceptionally well, with a modest deviation at higher fluid densities.
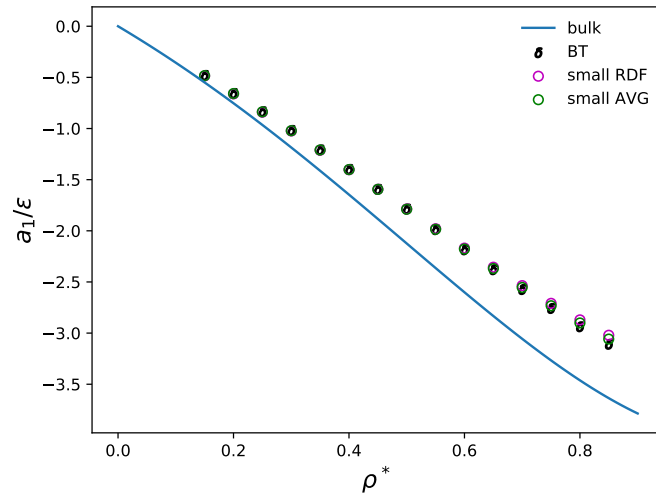
Figure 4.17: The bulk and small a_1 from BHPT are plotted together with the a_1 obtained from the BT RDFs at a confinement radius of $R = 10\sigma$. Small RDF a_{RDF} is obtained using Equation 2.36 while small AVG a_{AVG} is obtained using LAMMPS. The error is plotted for a_{AVG} with two standard deviations, but the error is so small it cannot be seen.

A short recap of the "bulk transformation" is that small a_1 can be predicted from bulk HS RDF, by simply having 1) a spherical and non-periodic ideal gas RDF g_0 and 2) the knowledge of the IC density at a certain ρ^*. Given that an analytical expression for the adsorption factor Γ as function of fluid density can be obtained, then small a_1 for spherical geometries of any (relatively large) R can be obtained from this bulk-transformation framework.

4.4   Reference system

The main observation from the previous sections is the existence of distinctive IC and OC regions inside fluids confined to spherical geometries of relative size. Perhaps the same reduction in density can model the small P_{HS} trend, such that the bulk CS EOS can be used in the following way

$$P_{\mathrm{HS,small}}\left(\rho^*\right) = P_{\mathrm{CS}}\left(\rho^*_{\mathrm{IC}}\right) \tag{4.11}$$

Given the case of $R = 10\sigma$ and by using the IC density obtained from Figure 4.14b, the following BT P_{HS} is obtained
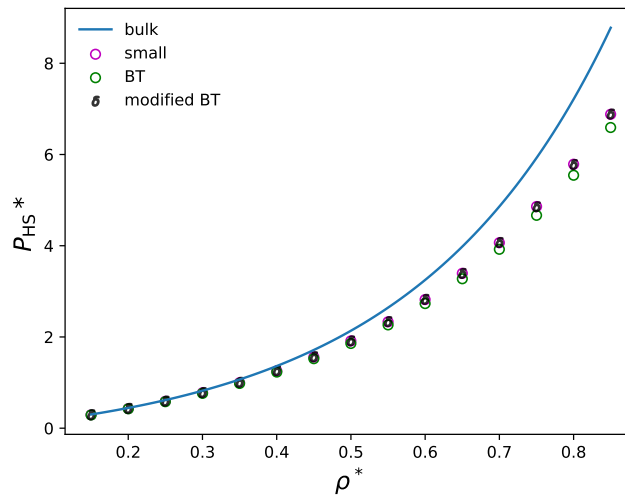
Figure 4.18: The Bulk HS and the small PHS pressure is plotted together with the pressure obtained from Equation 4.11 and 4.12 using the IC and modified IC density at $T^* = 1.5$ and $R = 10\sigma$. The bulk HS pressure HS pressure is obtained from the CS EOS and the small PHS pressure is obtained from LAMMPS.

By simply using the CS EOS with IC density values, a relatively accurate approximation for the small HS pressure can be obtained. At the same time, one can clearly observe a deviation between the BT and small pressure with increasing density. The difference can be caused by inaccurate IC density values and additional finite-size effects. Given that the error is only caused by inaccurate IC density values, then the IC density can be shifted by a constant k_1 to more accurately represent the small PHS pressure

$$P_{\mathrm{HS,small}}\left(\rho^*\right) = P_{\mathrm{CS}}\left(\rho^*_{\mathrm{IC}} \times k_1\right) \tag{4.12}$$

The constant is found to have the small value of $k_1 \approx 1.0143$ by using a simple Fsolve scheme, such that the modified BT pressure is plotted in Figure 4.18, and is shown to have excellent match with the small-system pressure. The significance of the low constant

k_1 magnitude suggest the difference between the unmodified BT and small pressure can solely be caused by inaccurate values of the IC densities. The modified BT PHS pressure is used together with the BT a_1 obtained from the previous section to accurately predict the small LJ/s pressure in Figure 4.19
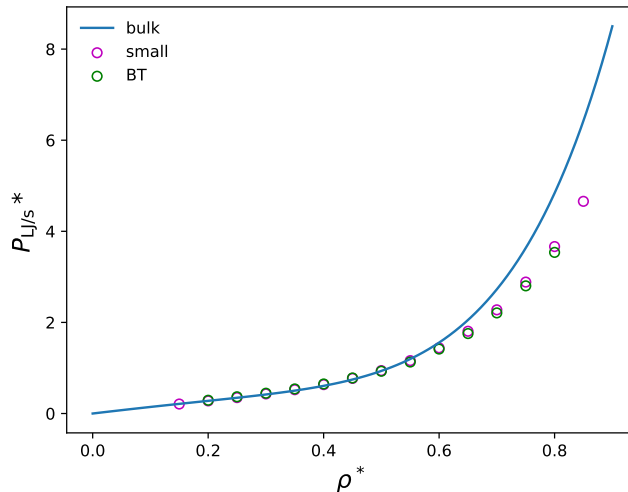
Figure 4.19: The bulk and small LJ/s pressure is plotted alongside the predicted LJ/s pressure with the use of BT a_1 and BT HS pressure from Equation 4.12. The bulk LJ/s pressure is obtained from BHPT of first order, while the small LJ/s pressure is obtained from LAMMPS.

The LJ/s pressure prediction is surprisingly accurate considering that only the first perturbation term is used. A possible reason can be due to the high fluid temperature $T^* = 1.5$, as LJ/s particles will behave more like HS with increasing temperature and the fact that perturbation terms are expanded in factors of $\beta = 1/(k_B T)$.

5 Conclusion

As stated in the introduction, the goal of this master thesis was to investigate the topic of Equation of State (EOS) that can describe the behaviour of nanofluids in spherical confinement. By taking basis in general Barker-Henderson perturbation theory (BHPT), this thesis has extended the theory by developing a framework that includes the description of finite-size effects that arises for fluids confined to systems of small size. With only a small number of modifications to the reference system and the first-order perturbation term a_1, the modified BHPT framework is observed to accurately predict small a_1 and small-system hard-sphere (HS) and Lennard-Jones/spline (LJ/s) pressures at low densities. While the predictive error increases with density, the error magnitude at high densities is still relatively limited.

A major finding in this thesis is the existence of a density arrangement region at the OC of the fluid that adsorbs and depletes particles from the IC region of the fluid. As a result of the particle adsorption, the IC density will decrease and be less than the overall fluid density. Since the majority of fluids in relatively large small-systems is made up of the IC-region, the IC density becomes a better descriptor of the fluid than the actual fluid density. Therefore, one can generally obtain a better description of nanofluids by simply using the IC density over the fluid density. For example, accurate predictive values of the small HS pressure can be obtained by simply using the CS EOS with IC densities, given that the IC densities are known. The knowledge of the IC density also considerably increases the accuracy of the bulk-small HS RDF transformation. The combination of the ρ_{IC}^* HS bulk RDF, the spherical non-periodicity effect and a normalization constant, predictive small a_1 can be obtained. Values of IC densities can be obtained from the adsorption per surface area Γ, which is relatively independent of R with the possible exception of low R. As a conclusion, by simply having the knowledge of the IC density and its variation with fluid density, an accurate BHPT EOS should be able to be obtained for fluids contained to small spherical regions of any (relatively large) R magnitudes.

6   Future Work

While the modified BHPT is observed to accurately predict the small-system LJ/s pressure, much remains to be done in order to be able to fully obtain a small LJ/s EOS for a fluid in spherical confinement of any arbitrary large radius R. The first task that should be done is to verify the qualitative conclusions made in this thesis by simulating actual HS particles in spherical confinement and increase the sampling number for ex. the density variation in Figures 4.10 and 4.14a. The second task is to investigate the temperature dependency of the small HS pressure and RDF, as the HS diameter $d_{\mathrm{BH}}(T^*)$ is defined to vary with temperature in BHPT. Given that all the thesis conclusions still holds, the next step is to obtain an accurate function for the IC density or adsorption per surface area Γ that depends on the fluid density and confinement size R. By obtaining such an analytical function, an accurate small LJ/s EOS can finally be obtained.

A natural step forward is to obtain various small LJ/s fluid properties from the EOS, including heat capacities and the vapor-liquid phase diagrams, and compare the results with bulk LJ/s and real fluid properties. The framework can also be applied to pair potential fluids such as LJ and various Mie pair potentials. Other highly relevant possibilities for further work include

- The comparison between the density arrangement region and Γ for fluids confined to spherical and planar walls. Given that a link between a spherical and planar wall can be obtained, then one can possibly use existing data from planar wall literature to spherically confined fluids.

- A more rigorous understanding for why small RDF and $a_{1,\mathrm{RDF}}$ can accurately reflect $a_{1,\mathrm{AVG}}$ and fluid properties. To the best of our knowledge, small RDFs have not been investigated in-depth in the current literature.

- The topic of fluids confined to small R geometries to the degree that the fluid become completely heterogeneous, as the current small BHPT EOS is only valid for "relatively large" small R geometries.

- The spherical small BHPT EOS framework can be extended to fluids in small systems of any type of confinement geometry, as adsorption should occur for hard walls of any type of confinement geometries. In this case the difficulty can be obtaining the non-periodic geometrical RDF reduction factor, especially for complex, non-symmetric confinement geometries.

References

[1] W.R. Smith and D. Henderson. Analytical representation of the percus-yevick hard-sphere radial distribution function. *Molecular Physics*, 19(3):411–415, 1970.

[2] Thomas Lafitte, Anastasia Apostolakou, Carlos Avendaño, Amparo Galindo, Claire S. Adjiman, Erich A. Müller, and George Jackson. Accurate statistical associating fluid theory for chain molecules formed from mie segments. *The Journal of Chemical Physics*, 139(15):154504, 2013.

[3] V. A. Bushman and V. E. Fortov. Equation of state. *A-to-Z Guide to Thermodynamics, Heat and Mass Transfer, and Fluids Engineering*, 2011.

[4] J. A. Barker and D. Henderson. What is "liquid"? understanding the states of matter. *Reviews of Modern Physics*, 48(4):587–671, Jan 1976.

[5] Otto. Redlich and J. N. S. Kwong. On the thermodynamics of solutions. v. an equation of state. fugacities of gaseous solutions. *Chemical Reviews*, 44(1):233–244, 1949.

[6] Ding-Yu Peng and Donald B. Robinson. A new two-constant equation of state. *Industrial & Engineering Chemistry Fundamentals*, 15(1):59–64, 1976.

[7] J. A. Barker and D. Henderson. Perturbation theory and equation of state for fluids. ii. a successful theory of liquids. *The Journal of Chemical Physics*, 47(11):4714–4721, 1967.

[8] Terrell L. Hill. *Thermodynamics of small systems.* Benjamin, 1964.

[9] Behnaz Rahmani Didar and I. Yucel Akkutlu. Pore-size dependence of fluid phase behavior and properties in organic-rich shale reservoirs. *SPE International Symposium on Oilfield Chemistry*, 2013.

[10] Xuezhen Wang, Lecheng Zhang, Yi-Hsien Yu, Lisi Jia, M. Sam Mannan, Ying Chen, and Zhengdong Cheng. Nano-encapsulated pcm via pickering emulsification. *Scientific Reports*, 5(1), 2015.

[11] Myroslav Holovko, Taras Patsahan, and Wei Dong. Fluids in random porous media: Scaled particle theory. *Pure and Applied Chemistry*, 85(1):115–133, Apr 2012.

[12] Holovko, Patsahan, and Shmotolokha. What is liquid in random porous media: the barker-henderson perturbation theory. *Condensed Matter Physics*, 18(1):13607, 2015.

[13] Leonardo Travalloni, Marcelo Castier, Frederico W. Tavares, and Stanley I. Sandler. Critical behavior of pure confined fluids from an extension of the van der waals equation of state. *The Journal of Supercritical Fluids*, 55(2):455–461, 2010.

[14] S. Plimpton. Fast parallel algorithms for short-range molecular dynamics. *Computational Physics*, Jan 1993.

[15] Jean-Pierre Hansen and Ian R. McDonald. *Theory of simple liquids.* Elsevier / Academic Press, 2007.

[16] Norman F. Carnahan and Kenneth E. Starling. Equation of state for nonattracting rigid spheres. *The Journal of Chemical Physics*, 51(2):635–636, 1969.

[17] Nathan Clisby and Barry M. Mccoy. Ninth and tenth order virial coefficients for hard spheres in d dimensions. *Journal of Statistical Physics*, 122(1):15–57, 2006.

[18] Michael L. Michelsen and Jørgen M. Mollerup. *Thermodynamic models: fundamentals & computational aspects.* Tie-Line Publications, 2018.

[19] J. Jover, A. J. Haslam, A. Galindo, G. Jackson, and E. A. Müller. Pseudo hard-sphere potential for use in continuous molecular-dynamics simulation of spherical and chain molecules. *The Journal of Chemical Physics*, 137(14):144505, 2012.

[20] Bjørn Hafskjold, Karl Patrick Travis, Amanda Bailey Hass, Morten Hammer, Ailo Aasen, and Øivind Wilhelmsen. Thermodynamic properties of the 3d lennard-jones/spline model. *Molecular Physics*, page 1–16, 2019.

[21] Robert W. Zwanzig. Erratum : High-temperature equation of state by a perturbation method. i. nonpolar gases. *The Journal of Chemical Physics*, 22(12):2099–2099, 1954.

[22] Thijs Van Westen and Joachim Gross. A critical evaluation of perturbation theories by monte carlo simulation of the first four perturbation terms in a helmholtz energy expansion for the lennard-jones fluid. *The Journal of Chemical Physics*, 147(1):014503, Jul 2017.

[23] Terrell L. Hill. *Thermodynamics of small systems two volumes bound in one.* Dover Publications, Inc, 2013.

[24] fix wall/region command - lammps documentation, https://lammps.sandia.gov/doc/fix_wall_region.html, accessed: 2020-05-17.

[25] Olav Galteland. Using lammps on sauron, "http://folk.ntnu.no/olavgal/spline/", accessed: 2020-06-02, Sep 2017.

[26] compute stress/atom command - lammps documentation, https://lammps.sandia.gov/doc/compute_stress_atom.html, accessed: 2020-05-17.

[27] Alexander Stukowski. Visualization and analysis of atomistic simulation data with ovito–the open visualization tool. *Modelling and Simulation in Materials Science and Engineering*, 18(1):015012, 2009.

[28] Seyed Hossein Jamali, Ludger Wolff, Tim M. Becker, Mariëtte De Groen, Mahinder Ramdin, Remco Hartkamp, André Bardow, Thijs J. H. Vlugt, and Othonas A. Moultos. Octp: A tool for on-the-fly calculation of transport properties of fluids with the order-n algorithm in lammps. *Journal of Chemical Information and Modeling*, 59(4):1290–1294, Nov 2019.

Appendix

A1   LAMMPS input scripts

Sample initialization script for LAMMPS. The number of TEMP0 for the number of particles and the confinement radius R. The PHS potential can be replaced with PAIR_STYLE LJ/SPLINE with PAIR_COEFF 1 1 1.0 1.0 1.0 0.0 to simulate LJ/s particles.

```
 1  log "log.LJ.init_random"
 2  variable dt equal 0.0003
 3  variable Nprod2 equal 10000000
 4  variable therm_print equal 100
 5  units lj
 6  atom_style full
 7  variable temperature equal 1.5
 8  region box2 sphere 0.0 0.0 0.0 temp0 units box units box
 9  region box sphere 0.0 0.0 0.0 temp0 units box units box
10  boundary f f f
11  create_box 1 box
12  create_atoms 1 random temp0 3688530 box2 units box
13  pair_style mie/cut 0.983917385243402
14  pair_coeff * * 1 0.9642390375385339 50.0 49.0 0.983917385243402
15  pair_modify shift yes
16  mass * 1
17  timestep ${dt}
18  neighbor 0.1 bin
19  neigh_modify every 1 delay 0 check yes
20  thermo_style custom step time etotal ke pe lx density temp press
21  thermo ${therm_print}
22  minimize 0.0 1.0e11 3000000 30000000
23  fix wall all wall/region box lj126 3.0 0.01 0.011224620483093731
24  fix_modify wall energy yes
25  minimize 0.0 1.0e-10 10000000 10000000
26  velocity all create 1.5 3068102
27  dump d_posen all custom 1000 "dump.LJs.nano.nvt" id type x y z
28  dump_modify d_posen sort id
29  fix ensNVT all nvt temp 1.5 1.5 $(100.0*dt)
30  fix 1 all wall/reflect xlo EDGE xhi EDGE ylo EDGE yhi EDGE zlo EDGE zhi EDGE
31  run ${Nprod2}
32  write_data "config.LJ.init_random"
```

Sample production run script for LAMMPS. Nprod steps is adjusted depending on the required statistical accuracy for the obtained results. The temp0 variables are replaced for the confinement radius R and the pressure calculation on line 28.

```
1   log "log.LJs.nano.nvt"
2   variable dt equal 0.0003
3   variable Nprod equal 20000000
4   variable therm_print equal 100
5   variable Nevery equal 250
6   variable Nrepeat equal 1
7   variable Nfreq equal ${Nevery}*${Nrepeat}
8   units lj
9   atom_style full
10  variable temperature equal 1.5
11  pair_style mie/cut 0.983917385243402
12  boundary f f f
13  read_data "config.LJ.init_random"
14  group SS type 1
15  fix 1 all wall/reflect xlo EDGE xhi EDGE ylo EDGE yhi EDGE zlo EDGE zhi EDGE
16  pair_coeff * * 1 0.9642390375385339 50.0 49.5 0.983917385243402
17  pair_modify shift yes
18  mass 1 1.0
19  timestep ${dt}
20  neighbor 0.1 bin
21  neigh_modify every 10 delay 0 check yes page 1000000 one 100000
22  thermo ${therm_print}
23  region box sphere 0.0 0.0 0.0 temp0 units box
24  fix wall all wall/region box lj126 3.0 0.01 0.011224620483093731
25  fix ensNVT all nvt temp ${temperature} ${temperature} $(100.0*dt)
26  compute peratom all stress/atom NULL
27  compute p all reduce sum c_peratom[1] c_peratom[2] c_peratom[3]
28  variable press equal -(c_p[1]+c_p[2]+c_p[3])/(3*(4/3)*PI*temp0*temp0*temp0)
29  fix o_tps all ave/time ${Nevery} ${Nrepeat} ${Nfreq} v_press file "out.entps_nvt"
30  dump d_posen all custom ${Nevery} "dump.LJs.nano.nvt" id type x y z
31  dump_modify d_posen sort id
32  dump d_check all custom ${Nprod} "dump_LJs.nano.check_nvt" id type x y z
33  run ${Nprod}
34  write_data "config.LJs.nano.end_nvt"
```

A2   Fortran scripts

```fortran
1    program density_variation
2          implicit none
3          integer, parameter :: n=temp1, it=400000, space=temp2
4          real, parameter:: radius=temp, dr=(2*radius)/(space-1)
5          integer :: i, j, k, z, dummy, it0=0
6          integer, dimension(space) :: h=0
7          real, dimension(space) :: r_vec = (/(i*dr, i=0,space-1)/), g=0
8          real, dimension(3,n) :: r=0
9          real, dimension(3) :: rij
10         real :: rij_sq, r_hi, r_lo, h_id, rho=n/((4.0/3.0)*4.D0*DATAN(1.D0)*radius**3), const
11         open(1, file='dump.LJs.nano.nvt')
12         do while (it0 < it)
13             do j = 1,9
14                 read(1,*)
15             end do
16             do i=1,n
17                 read(1,*)dummy,dummy,rij(1),rij(2),rij(3)
18                 r(:,i) = (/rij(1), rij(2),rij(3)/)
19             end do
20             do i = 1, n-1
21                 rij_sq = sum(r(:,i)**2)
22                 k = floor(sqrt(rij_sq)/dr) + 1
23                 h(k) = h(k) + 1
24             end do
25             it0 = it0+1
26         end do
27         const = 4.0*4.D0*DATAN(1.D0)/ 3.0
28         do k = 1, space
29             g(k) = real(h(k))/real(it)
30    h_id = const*((r_lo + dr)**3 - (real(k-1)*dr)**3)
31             g(k) = g(k)/h_id
32         end do
33         open (unit=2,file="temp-dens.txt",action="write",status="replace")
34         do z = 1, space/2
35             write(2,fmt='(2f15.8)') r_vec(z), g(z)
36         end do
37         close(1)
38         end program read
```

```fortran
1    program RDF
2          implicit none
3          integer, parameter :: n=temp, it=80000, space=temp2
4          real, parameter:: radius=temp, dr=(2*radius)/(space-1)
5          integer :: i, j, k, z, dummy, it0=0
6          integer, dimension(space) :: h=0
7          real, dimension(space) :: r_vec = (/(i*dr, i=0,space-1)/), g=0
8          real, dimension(3,n) :: r=0
9          real, dimension(3) :: rij
10         real :: rij_sq, r_hi, r_lo, h_id, rho=n/((4.0/3.0)*4.D0*DATAN(1.D0)*radius**3), const
11         open(1, file='dump.LJs.nano.nvt')
12         do while (it0 < it)
13               do j = 1,9
14                     read(1,*)
15               end do
16               do i=1,n
17                     read(1,*)dummy,dummy, rij(1),rij(2),rij(3)
18                     r(:,i) = (/rij(1), rij(2), rij(3)/)
19               end do
20               do i = 1, n-1
21                     do j = i+1, n
22                           rij(:) = r(:,i)-r(:,j)
23                           rij_sq = sum(rij**2)
24                           k = floor(sqrt(rij_sq)/dr) + 1
25                           h(k) = h(k) + 2
26                     end do
27               end do
28               it0 = it0+1
29         end do
30         const = 4.0*4.D0*DATAN(1.D0)*rho/ 3.0
31         do k = 1, space
32               g(k) = real(h(k))/real(n*it)
33               h_id = const*((r_lo + dr)**3 - (real(k-1)*dr)**3)
34               g(k) = g(k)/h_id
35         end do
36         open (unit=2,file="rdf.txt",action="write",status="replace")
37         do z = 1, space
38               write(2,fmt='(2f15.8)') r_vec(z), g(z)
39         end do
40         close(1)
41         end program read
```

A3   Python scripts

```python
1   # calculating a1_RDF
2   import numpy as np
3   import math
4   from scipy.interpolate import interp1d
5   from pathlib import Path
6
7
8   def spline(z):
9       rs = (26 / 7) ** (1 / 6)
10      rc = 67 / 48 * rs
11      a = -(24192 / 3211) * (1 / (rs ** 2))  # (-24192/3211)*(1/rs**2)
12      b = -(387072 / 61009) * (1 / (rs ** 3))  # (-387072/61009)*(1/rs**3)
13      if z <= rs:
14          return 4 * (1 / (z ** 12) - 1 / (z ** 6))
15      if rs < z < rc:
16          return a * (z - rc) ** 2 + b * (z - rc) ** 3
17      if rc <= z:
18          return 0
19
20  def numint2(f, a, b):
21      x, w = np.polynomial.legendre.leggauss(16)
22      t = 0.5 * (x + 1) * (b - a) + a
23      return sum(w * f(t)) * 0.5 * (b - a)
24
25
26  dens = temp
27  data = np.loadtxt("rdf.dat")
28  ip = interp1d(data[1:,0],data[1:,0]**2*np.vectorize(spline)(data[1:, 0])*data[1:,1], kind='cubic')
29  rs = (67/48)*(26/7)**(1/6)
30  a000 = numint2(np.vectorize(ip),1,rs)*dens*2*math.pi
31
32  f = open("a1rdf.txt","w+")
33  f.write("temp␣␣␣" + str(a000))
34  f.close()
```